

Investigating the origin of radio emission in candidate super-Eddington accreting black holes

M. Gendron-Marsolais^{1,2}, P. Marziani^{3,1}, M. Berton⁴, E. Järvelä⁵, A. del Olmo¹, M. Sargent⁶, M. D’Onofrio⁷, L. Crepaldi^{7,8}, A. Damas-Segovia⁹, B. Punsly¹⁰, and L. Verdes-Montenegro²

¹ Instituto de Astrofísica de Andalucía, Glorieta de Astronomía, Granada, IAA-CSIC, Spain
e-mail: mlgem@ulaval.ca

² Département de physique, de génie physique et optique, Université Laval, Québec (QC), G1V 0A6, Canada

³ Istituto Nazionale di Astrofisica, Osservatorio di Padova, Vicoletto dell’Osservatorio 5, 35122, Padova, Italy

⁴ European Southern Observatory (ESO), Alonso de Córdoba 3107, Casilla 19, Santiago 19001, Chile

⁵ Department of Physics and Astronomy, Texas Tech University, Box 41051, Lubbock 79409-1051, TX, USA

⁶ Institute of Physics, Laboratory of Astrophysics, École Polytechnique Fédérale de Lausanne (EPFL), Observatoire de Sauverny, Versoix CH-1290, Switzerland

⁷ Dipartimento di Fisica e Astronomia “G. Galilei”, Università di Padova, Vicoletto dell’Osservatorio 3, 35122, Padova, Italy

⁸ Istituto Nazionale di Astrofisica, Osservatorio di Cagliari, Via della Scienza 5, 09047, Selargius, Italy

⁹ Max-Planck-Institut für Radioastronomie, Auf dem Hügel 69, 53121 Bonn, Germany

¹⁰ ICRA, Physics Department, University La Sapienza, Roma, Italy

Received ...

ABSTRACT

Context. Recent works show that the radio power of quasars accreting at very high rates can reach surprisingly high values. These studies suggest that this radio emission might originate from star formation, but lack of data leaves open the possibility that they could also contain a jetted active galactic nucleus (AGN).

Aims. We investigate the origin of the radio emission of a sample of 18 super-Eddington candidates, over a wide range of redshifts. These sources are expected to have extreme radiative output per unit black hole mass, show high-velocity outflows and are therefore thought to be a prime mover of galactic evolution via radiative and mechanical feedback.

Methods. We present new Karl G. Jansky Very Large Array (VLA) observations at L, C and X-band of these sources, which we combine with observations from the LOw-Frequency ARray (LOFAR) Two-metre Sky Survey (LoTSS) and the Very Large Array Sky Survey (VLASS). We also use optical and IR data to derive estimates of accretion and wind parameters, as well as star formation rates to compare with the ones derived from the radio emission.

Results. Based on the radio variability, luminosity, morphology, radio spectral properties, radio vs IR estimates of star formation rate and radio-to-mid IR flux ratio, we find that 7 of our 18 targets are likely to have their radio emission predominantly coming from SF, and 6 from a combination of SF and AGN-related mechanisms, while only three sources indicate a core or jetted AGN only origin for the detected radio emission. This is consistent with previous studies, and supports the prevalence of lower power radio structures associated with star-forming activity rather than relativistic jets in the high Eddington ratio regime. In the same sample, however, we find three sources for which the data suggest a concomitant presence of super-Eddington accretion and relativistic ejections.

Key words. quasars: general – Galaxies: jets – Galaxies: star formation

1. Introduction

The main sequence (MS) of quasars is a classification scheme based on the spectral properties of quasars, most commonly represented by the plane between the intensity ratio $R_{\text{FeII}} = W(\text{FeII}4570)/W(\text{H}\beta)$ (where $W(\text{FeII}4570)$ is the equivalent width of the blend of multiplets between 4434 Å and 4684 Å and $W(\text{H}\beta)$ the equivalent width of the broad component of the $\text{H}\beta$ emission line) and the full width at half maximum (FWHM) of the $\text{H}\beta$ emission line. It is a powerful analysis tool of the observational properties of type 1 active galactic nuclei (AGN, e.g., Sulentic et al. 2000a; Marziani et al. 2018). The relevance of the MS for quasar astronomy is that several observational and physical properties, such as the ones related to the prominence of outflows and the prevalence of jetted sources, change systematically along the MS. There is a growing consensus that the main factors shaping the MS are the Eddington ratio (L/L_{Edd})

and the viewing angle, defined as the angle between the line-of-sight and the symmetry axis of the AGN (e.g., Panda et al. 2019). Quasars can be divided into two broad populations based on their position in the MS : Population A (narrower $\text{H}\beta$ lines, with $\text{FWHM} < 4000 \text{ km s}^{-1}$) and B (broad $\text{H}\beta$ lines, with $\text{FWHM} > 4000 \text{ km s}^{-1}$). The sub-population of quasars located towards the high R_{FeII} end of the MS (extreme Population A, or xA for brevity) are characterized by extreme observational parameters and are linked to high Eddington ratio (Marziani & Sulentic 2014; Du et al. 2016). They show a distinctive UV spectrum that makes them easily recognizable even at high z (Martínez-Aldama et al. 2018). The highest radiators per unit mass should be preferentially found at high z , as this indeed seems to be the case: the most luminous, intrinsically blue quasar population composite spectra closely resemble the highest radiator UV spectra at low- and moderate z (Nardini et al. 2019). They are believed to be in their early stage of evolution (Mathur 2000), and

they may constitute the dominant source of ionizing photons in the reionization epoch.

A recent analysis has shown that radio powers can reach surprisingly high values in xA objects (Ganci et al. 2019), some entering the radio-loud (RL) regime, that is with a Kellermann’s parameter (defined as the ratio R_k between radio flux density at 5 GHz and the optical flux density at 5100 Å, Kellermann et al. 1989), above 10. The strong radio emission from RL sources is typically associated with the presence of a relativistic jet, whereas in radio-quiet (RQ) sources the jet is expected to be non-relativistic or intrinsically weaker than in RL. Star formation (SF) is considered an important agent especially at lower power and lower frequencies: the fraction of star-forming galaxies is increasing at fluxes below $S_{1.4\text{ GHz}} \simeq 10\text{ mJy}$ (e.g., Condon 1989; Smoli et al. 2017; Mancuso et al. 2017), although other mechanisms more closely related to the AGN have been proposed.

However, despite their high radio powers, the sample of strong FeII emitters from (Ganci et al. 2019) obeys to the FIR-radio correlation for star-forming galaxies and RQ quasars. Moreover, a large fraction (75%) of radio-loud narrow-line Seyfert 1s (RL NLSy1s) shows mid-IR emission properties consistent with SF being the dominant component also in radio emission (Caccianiga et al. 2015; Järvelä et al. 2022). Therefore, it is legitimate to suggest that the radio emission from most sample sources in Ganci et al. (2019) is dominated by processes not related to the AGN. Nonetheless, the lack of data leaves open the possibility that they could also harbor a relatively low radio-power relativistic jet or outflow. This would be the case if they were sources with relatively low black hole mass, as jet power scales nonlinearly with black hole mass (Heinz & Sunyaev 2003). Indeed, in recent years a number of objects characterized by prominent FeII emission and formally RQ have been classified as jetted (e.g., Lähteenmäki et al. 2018; Berton et al. 2018, 2020; Järvelä et al. 2021; Marziani et al. 2021; Vietri et al. 2022).

Mrk 231, a low- z , high- L prototypical xA source, is one of the RL sources from the Ganci et al. 2019 sample. Mrk 231 has been described by Sulentic et al. (2006) as a high- L , highly accreting quasar misplaced at late cosmic epochs. Emission line properties are extreme, in terms of FeII emission, CIV $\lambda 1549$ blueshift, and blueward asymmetry of H β . It is a broad absorption line (BAL) QSOs suffering some internal extinction and with extreme absorption troughs in radial velocity (Sulentic et al. 2006; Veilleux et al. 2016). Mrk 231 is known to possess an unresolved core, highly variable and of high brightness temperature (Condon et al. 1991). Superluminal radio components of Mrk 231 have been detected, and the relation between BALs, radio ejections, and continuum change (Reynolds et al. 2017), illustrating the complex interplay of thermal/nonthermal nuclear emission that can be perhaps typical of sources accreting at extremely high rates. Still, according to the location in the diagram of Ganci et al. 2019, the dominant emission mechanism is SF. This inference is consistent with the enormous CO luminosity of the AGN host (Rigopoulou et al. 1996).

Mrk 231 notwithstanding, the wide majority of extreme radiators remains little studied, and this is especially true as far as their radio properties are concerned. Strong FeII emitters are known to have high accretion rate, possibly at a super-Eddington level (Du et al. 2016), although their radiative output is expected to remain within a factor ~ 2 above the Eddington limit (Mineshige et al. 2000). High L/L_{Edd} can coexist with powerful jetted radio emission ($\log P_v > 10^{31}\text{ erg s}^{-1}\text{ Hz}^{-1}$). There is no physical impossibility in this respect (Czerny et al. 2018), and re-

cent works consider the relativistic jet and non-relativistic wide angle outflows as two aspects of a hydromagnetically-driven wind (Reynolds et al. 2017). Concomitant high accretion and high radio power are observed in compact steep-spectrum (CSS) radio sources (e.g., Wu 2009). General relativistic magnetohydrodynamic simulations also can reproduce high L/L_{Edd} sources with jets (McKinney et al. 2017; Liska et al. 2022). Our view is likely biased by the relative rarity of this sort of sources at low- z (O’Dea 1998), and especially by the scarcity of high-quality UV/optical spectra, and their rather sketchy interpretation that, in the past, ignored the MS trends. The basic issue is whether the RL sources in the xA spectral bins of the MS are truly jetted (as RL NLSy1s are, Foschini et al. 2015) or dominated by radio emission from SF.

Generally speaking, RL extreme accretors may appear indistinguishable in the H β spectral range from their RQ counterparts, as both RQ and RL strong-FeII show a large blueshift in their [O III] profiles (Bertone et al. 2016; Bertone & Järvelä 2021). The radio power may be associated with a relatively small black hole mass. They could be systems in their early stage of evolution for which a spin-up has been made possible by a recent accretion event (Mathur 2000; Sulentic et al. 2000a), but the possibility of radio emission due to SF calls into question the radio-mode AGN feedback as a cosmologically relevant process in massive galaxy formation. This class of sources is believed to be representative of highly accreting quasars observed at very early cosmic epoch, as indeed proved by the NLS1-like object recently discovered at $z = 6.56$ (Wolf et al. 2023). Sources in the re-ionization epoch may be both accreting at super-Eddington rates, and their associated starburst be the primary source of ionizing photons (e.g., Decarli et al. 2017). Several highest- z quasars have been detected in the radio, implying extremely powerful radio emission (e.g., Belladitta et al. 2019). Which is however the main culprit, SF or black hole activity? Establishing their relative contribution in high accretors is expected to provide strong constraints on the ability of nuclear activity to provide the main source of ionizing photons at re-ionization epoch.

In this work we analyze the observations carried out with the Karl G. Jansky Very Large Array (VLA) of a sample of 18 xA sources with intensity ratio $R_{\text{FeII}} \gtrsim 1$ taken from Marziani et al. (2003); Sani et al. (2010) and Ganci et al. (2019). We add observations from radio surveys as well as optical and IR data to complete our analysis and determine the origin of the radio emission. In Section 2, we present the sample and the data reduction process, while the analysis of these datasets is presented in section 3. We discuss our findings in section 4 and provide a summary of our results in section 5. Appendix C includes an analysis of optical and IR data relevant for the interpretation of the radio observations. We adopted $H_0 = 70\text{ km s}^{-1}\text{ Mpc}^{-1}$, $\Omega_M = 0.3$ and $\Omega_{\text{vac}} = 0.7$.

2. Sample selection and data reduction

Our complete sample is shown in Table 1 and contains a total of 18 sources that according to their optical spectra are classified as xA objects in the MS, that is with $R_{\text{FeII}} \gtrsim 1$. Throughout the text, we will refer to the sources by their short names as defined in column 2 of Table 1. We stress again that this condition is thought to be associated with black holes of highest radiative output per unit black hole mass (e.g., Marziani et al. 2001; Sun & Shen 2015; Du et al. 2016; Panda et al. 2019; Marziani et al. 2025). Among them, several show multi-frequency evidence of extraordinary activity level which may be ascribed to super-Eddington accretion (Marziani et al. 2025, and references therein). Five of

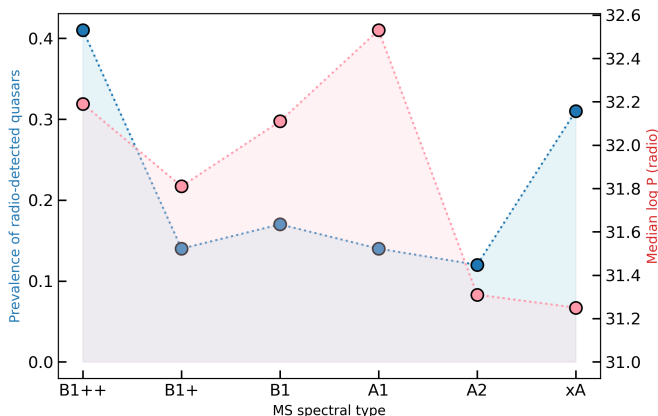


Fig. 1: Prevalence of FIRST-detected type-1 AGN (Marziani et al. 2013) (blue circles and cyan shading) and median radio power (red circles and rose shading) as a function of spectral type along the quasar main sequence.

these sources were taken from radio survey Ganci et al. (2019) and the rest are supplemented by low z sources from Sani et al. (2010) and Marziani et al. (2003) detected in FIR.

In optically selected quasar samples, RL sources tend to concentrate at the two ends of the MS. Figure 1 illustrates the incidence and the radio power as a function of the spectral types along the quasar MS, for FIRST detected sources in the sample of (Marziani et al. 2013). The B spectral types are where most powerful radio sources are found; if they are observed pole-on, they appear as core-dominated with narrower lines that let them populate part of spectral type A1 (Wills & Browne 1986; Jarvis & McLure 2006; Ganci et al. 2019). The surprising result is that in correspondence of the xA spectral type there is a threefold increase in the prevalence of radio detected sources. In this case, however, the radio power is systematically much lower.

The properties of radio emission found in one domain such as the xA regime defined by $R_{\text{FeII}} \gtrsim 1$ (spectral types A3 and A4; see Sulentic et al. 2002) can be generalized to other sources with similar spectral characteristics. However, these results do not extend to quasars of markedly different spectral types along the MS, particularly those in the extreme end of Population B. In simple terms, Population B sources may exhibit comparable radio power to xA quasars, yet the origin of that radio emission could be fundamentally different—most likely jet-driven (Zamfir et al. 2008; Ganci et al. 2019).

An additional consideration in interpreting these data concerns the spatial origin of the far-infrared emission. Relativistic jets are nuclear phenomena, and the presence of radio lobes corroborates jet activity, whereas star formation can be nuclear, circum-nuclear, or distributed across the host. Because the available measurements do not spatially resolve the FIR emission attributed to star formation, a contribution from a mildly beamed (i.e., weakly Doppler-boosted) or misaligned relativistic jet cannot be ruled out.

2.1. VLA data

The radio observations presented in this paper are from the VLA project 20B-081 (PI: M. Berton). There are 17 datasets in total - each including a single target, except one of them, which includes two sources, J1209+5611 and J1301+5902. The observations were all taken from 2020-12-04 to 2020-12-08, in three

bands: L (1.5 GHz), C (5 GHz), and X (10 GHz). Due to the COVID pandemic, the data were taken in a non-standard configuration, with two arms fully extended in A-configuration and one arm in the more compact B-configuration except for one antennae moved to the end position of the arm. Fig. A.2 shows the antenna positions during the observations of J00418+4021 on 2020-12-04, and the associate uv plane coverage of the L-band scan. Such non-uniform configuration might have impacted the quality of some of the images (slightly elongated synthesized beam), but overall we do not note a significant impact: the rms noise is consistent with the expected values. For L-band, we used the 8-bit samplers with center frequencies 1.25 and 1.75 GHz, for C-band, the 8-bit samplers centered at 4.72 and 5.75 GHz, and for X-band, two 3-bit samplers centered at 9 and 11 GHz. Each target was observed for a total of 10 minutes per band, which accounting for amplitude and phase calibration and overheads correspond to 20 minutes per band.

We applied the CASA (CASA Team et al. 2022) pipeline version 6.4.1.12 to each dataset. The pipeline outputs were visually inspected to make sure the pipeline ran well on all datasets. Once calibrated, the target observations were split away for each band in individual measurement sets. We did not perform any (time or frequency) averaging. Each was imaged individually using `TCLEAN` from CASA (version 6.5.2.26). We used 2 Taylor coefficients to model the emission's spectral structure across the band and applied W-projection corrections with 14, 4 and 2 planes (for the L, C and X-band, respectively) to correct for the wide-field, non-coplanar baseline effect (Cornwell et al. 2008). We chose cell sizes of $0.2''$, $0.07''$ and $0.03''$ for the L, C and X-band images, respectively, and image sizes of $9000 \text{ pixels} \times 9000 \text{ pixels} = 30' \times 30'$, $7500 \text{ pixels} \times 7500 \text{ pixels} = 8.75' \times 8.75'$ and $9000 \text{ pixels} \times 9000 \text{ pixels} = 4.5' \times 4.5'$ (approximate sizes of the full width at half maximum of the field of view at the respective frequencies). Due to the presence of very bright sources near J11292-0424, J15455+4846 and J17014+5149, we increased the size of the L-band image which improved significantly the image quality. We used the multi-scale `CLEAN` algorithm from Cornwell (2008) to probe the different scales of the structures in the images: 0, 5 and 15 pixels. Briggs weighting is used with a default robust factor of 0.5 (which corresponds to an intermediate between natural and uniform weighting). We run a round of phase self-calibration to improve the overall dynamic range in two cases: for J11292-0424, whose field encompassed the brightest source, and for 12562+5652, which is the brightest target. Finally, wideband primary beam corrections were calculated with the CASA task `WIDEBANDPBCOR`, listing all the spectral windows and the middle channel. Cutouts of the final images are shown in Fig. A.1, while the obtained beam sizes, rms and dynamic ranges (DR) are listed in Table B.1. The noise level in each image has been evaluated by taking the average of the rms noise in the four corners of the cutouts, so near the sources, but in regions devoid of other bright radio sources. On average, the rms reached are ~ 30 , 10 and $8 \mu\text{Jy}/\text{beam}$ for the L, C and X-band images (which are close to the noise expected for such observations based on the VLA exposure calculator), except for the case of J12562+5652, whose brightness limits the noise reachable. Flux densities encompassed in 5 sigma contours (or peak flux densities for compact sources) are listed in Table B.2. To test the robustness of these measurements, we compared them with integrated flux densities derived from 2D Gaussian fits. We used the CASA task `IMFIT` to test this, and obtained values within $\pm 5\%$ from the 5 sigma contours method for the sources with an elliptical morphology, confirming the validity of this approach. For flux calibration we assume a relative error of 5% for all VLA

Table 1: Targets of the sample

NED Alias	Short name	z	RA (2000)	Dec (2000)	Opt.	FIR
Mrk 957	J00418+4021	0.071	00h41m53.420	+40d21m17.29s	HO87	IRAS, ISO, AKARI
PG0043+039	J00457+0410	0.385	00h45m47.225s	+04d10m23.38s	M03	IRAS
IZw1	J00535+1241	0.059	00h53m34.920s	+12d41m35.87s	M22	IRAS, ISO, MIPS, AKARI
Mrk 142	J10255+5140	0.045	10h25m31.279s	+51d40m34.85s	M03	IRAS, MIPS
Mrk 1298	J11292-0424	0.062	11h29m16.729s	-04d24m07.26s	M03	IRAS, MIPS, AKARI
WISEA J114201.86+603029.7	J11420+6030	0.718	11h42m01.847s	+60d30m30.23s	SDSS	...
SDSS J120734.63+150643.6	J12075+1506	0.750	12h07m34.631s	+15d06m43.70s	SDSS	...
SDSS J120910.62+561109.6	J12091+5611	0.453	12h09m10.620s	+56d11m09.30s	SDSS	...
SDSS J123640.33+563021.6	J12366+5630	0.698	12h36m40.346s	+56d30m21.43s	SDSS	...
Mrk 231	J12562+5652	0.042	12h56m14.222s	+56d52m25.10s	M03	IRAS, ISO, MIPS, AKARI, PACS
SBS 1259+593	J13012+5902	0.476	13h01m12.933s	+59d02m06.75s	M22	IRAS, ISO, MIPS
FBQS J1405+2555	J14052+2555	0.164	14h05m16.218s	+25d55m34.12s	M22	IRAS, ISO, MIPS
PG 1404+226	J14063+2223	0.098	14h06m21.890s	+22d23m46.51s	M22	IRAS, MIPS
PG 1415+451	J14170+4456	0.114	14h17m00.825s	+44d56m06.33s	M22	IRAS, ISO, MIPS
SDSS J142549.19+394655.0	J14258+3946	0.505	14h25m49.190s	+39d46m55.00s	SDSS	...
SDSS J144733.05+345506.7	J14475+3455	0.662	14h47m33.052s	+34d55m06.82s	SDSS	IRAS
PG 1543+489	J15455+4846	0.401	15h45m30.237s	+48d46m09.00s	M22	IRAS, ISO, MIPS
PG 1700+518	J17014+5149	0.292	17h01m24.898s	+51d49m20.38s	M03	IRAS, ISO, MIPS

Notes. Column 1: NED Alias. Column 2: Short name. Column 3: redshift. Column 4 and 5 : coordinates. Column 6: Source of optical spectra: HO87: [Halpern & Oke 1987](#); M03: [Marziani et al. 2003](#); M22: [Marziani et al. 2022](#); SDSS: Sloan Digital Sky Survey. Column 7: Source of IR. MIPS: Multiband Imaging Photometer; PACS: Photodetector Array Camera and Spectrometer.

bands¹. The uncertainties is then given by the sum in quadrature of the rms and the calibration error. Of the 18 sources observed with the VLA, 17 are detected at X-band and 16 at L and C-band. For undetected sources, we indicate a 5 sigma upper limit in Table B.2.

2.2. Complementary radio data

In order to complement our VLA observations, we added to the analysis radio observations from the Low-Frequency ARray (LOFAR) Two-metre Sky Survey (LoTSS) DR2 ([Shimwell et al. 2022](#)) and the Very Large Array Sky Survey (VLASS) ([Lacy et al. 2020](#)).

We looked for our sources in LoTSS DR2 by first identifying the full bandwidth Stokes I continuum mosaic (with a central frequency of 144 MHz) that better covers each targets and downloaded the fits file of the full resolution image. Cutouts around the sources are presented in Fig. A.1, while the beam sizes, rms and DR of the mosaic are listed in Table B.1. We determined the noise level in the same way as for the VLA images, by taking the average of the rms noise in the four corners of the cutouts. LOFAR images have beam sizes of $6'' \times 6''$ and an average noise of about 0.1 mJy/beam. All 10 sources covered by LoTSS DR2 are detected. Flux densities encompassed in 5 sigma contours (or peak flux densities for spatially unresolved sources) are listed in Table B.2. We assumed a relative error of 10% on the flux calibration ([Shimwell et al. 2022](#)) and the uncertainties on the fluxes are then given by the sum in quadrature of the rms and the calibration error.

¹ The Flux density scale calibration accuracy is based on the VLA Observational Status Summary 2020B.

We obtained the VLASS images (with central frequency of 3 GHz) encompassing our sources through the Canadian Astronomy Data Centre (CADC) portal. All sources are covered by the survey, either in Quick Look (QL) or Single Epoch (SE) continuum images, in at least two epochs. We selected SE images when available to extract the flux, as they are intended to be the reference continuum images for each epoch of VLASS, and otherwise the QL image from the epoch closest in time to the VLA observations (see column 8 in Table B.1). The images have beam sizes of about $2 - 4''$ and an average noise of about 0.1 mJy/beam. Flux densities encompassed in 5 sigma contours (or peak flux densities for spatially unresolved sources) are listed in Table B.2. We assumed a relative error of 3 and 10% on the flux calibration for SE and QL images, respectively, and the uncertainties on the fluxes are then given by the sum in quadrature of the rms and the calibration error. We additionally extracted the flux from all epochs and plotted for each source their flux variation on Fig. A.3. For sources with detections in at least two epochs, we computed the variability index using the formula adopted from [Aller et al. \(1992\)](#):

$$V = \frac{(S_{\max} - \sigma_{S_{\max}}) - (S_{\min} + \sigma_{S_{\min}})}{(S_{\max} - \sigma_{S_{\max}}) + (S_{\min} + \sigma_{S_{\min}})}, \quad (1)$$

where S_{\max} and S_{\min} are the maximum and minimum values of the flux density over all epochs of observations, while $\sigma_{S_{\max}}$ and $\sigma_{S_{\min}}$ are their associated errors. These are shown on Fig. A.3. Negative values of V correspond to cases where the error is greater than the observed scatter of the data. Three of our sources exceed the value of $V = 0.1$, which makes them potential candidates for variable objects (e.g. [Kunert-Bajraszewska et al. 2025](#)): J12091+5611, J12562+5652 and J15455+4846. For these sources, the flux extracted from the SE image has been selected for the rest of the analysis, and we verified that it also

correspond to the epoch closest in time with the VLA observations.

2.3. Optical and IR data

The optical data come from three main sources: the [Marziani et al. \(2003\)](#) atlas of low- z type-1 AGN covering the H β spectral range; the [Marziani et al. \(2022\)](#) comparative analysis, where the H β spectral range was paired to the rest frame UV blend at $\lambda 1900$, and the SDSS. In addition, the spectrum of J00418+4021 was digitized from a published plot ([Halpern & Oke 1987](#)). Continuum S/N is $\gtrsim 20$ excluding J00418+4021. Spectral resolution is $\lambda/\delta\lambda \sim 2000$ for the SDSS data, $\lambda/\delta\lambda \sim 1000$ for the other spectra. The SDSS spectra and [Marziani et al. \(2003\)](#) were fit for this work using the same multi-component, non-linear analysis employed in [Marziani et al. \(2022\)](#). A special attention was devoted in this work to the fitting of the [OIII] $\lambda\lambda 4959, 5007$ lines, as well as in the detection of a possible blueshifted (outflow) component in H β . Appendix C reports the results of a multicomponent nonlinear analysis of the H β and [OIII] $\lambda 5007$ lines. Accretion parameters (Eddington ratio and black hole mass estimates derived from optical spectra) are also reported in Appendix C.

We used IR fluxes extracted from the Wide-field Infrared Survey Explorer (WISE, [Wright et al. 2010](#)), as well as FIR fluxes from the Infrared Astronomical Satellite (IRAS) Survey ([Neugebauer et al. 1984](#)) – except for source J14063+2223, which did not have IRAS data at $100\ \mu\text{m}$, so we used the flux from the Infrared Space Observatory (ISO) survey ([Kessler et al. 1996](#)). IR and FIR fluxes used during the analysis are reported in table B.3. We considered also AKARI ([Murakami et al. 2007](#)), ISO, Spitzer MIPS, and Herschel data. The AKARI fluxes at $60\mu\text{m}$ are available for only 4 objects (listed in Table 1), and are about $\approx 20\%$ lower than the IRAS fluxes, as expected from the comparison to more precise data from newer telescopes ([Serjeant & Hatziminaoglou 2009](#)). We therefore expect that the SFR should be consistent with the ones derived from IRAS data, for the same normalization used in Section 3.4.

3. Results

3.1. Radio loudness

We start by calculating the Kellermann's parameter R_K ([Kellermann et al. 1989](#)), using the radio flux density at 1.4 GHz and the optical flux density at $5100\ \text{\AA}$ from column 2 in Table C.1. The observed radio flux density $f_{v,o}$ reported in Table B.2 has been converted to rest frame by applying a K-correction: $f_{v,e} = f_{v,o}[(1+z)^{(-\alpha+1)}]$ ([Ganci et al. 2019](#)), where the spectra index α is reported in sixth column of Table B.4. We use the following criteria to distinguish between radio loud and radio quiet sources:

- Radio loud (RL): sources with $R_K \geq 10$, from the radio fluxes at 1.4GHz reported in Table B.2, and from the optical fluxes at $5100\ \text{\AA}$ (Appendix C);
- Radio quiet (RQ): sources with $R_K < 10$.

This criterion applied to our sample yields a large fraction of RL sources, 8 out of 18. We note however that $R_K \geq 10$ is not by itself a sufficient condition to demonstrate the presence of a relativistic jet, especially among xA quasars ([Zamfir et al. 2008; Ganci et al. 2019](#)). If a more restrictive condition $\log R_K \geq 1.8$ (corresponding to $R_K \geq 70$) is applied as suggested by [Zamfir et al. \(2008\)](#) for the lower boundary of the RL phenomenon when

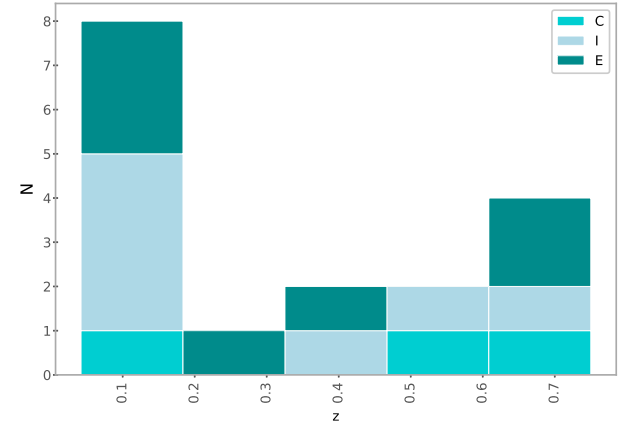


Fig. 2: Radio morphology distribution across the redshifts of the sources. C indicates compact at all frequencies observed, I is intermediate morphology detected in at least one band, and E indicates the presence of diffuse emission in at least one band.

analysing FRII sources, only J00418+4021 and J14258+3946 would be classified as RL. We also note that the optical continuum of J00418+4021 might have been underestimated, making J14258+3946 the sole bona-fide RL source of the sample.

3.2. Radio morphology

Following [Berton et al. \(2018\)](#), we define three morphological classes reflecting the properties of the sources seen in the maps, using the ratio (\mathcal{R}) of the peak to the total flux density of each source:

- Compact: sources with $\mathcal{R} \geq 0.95$, labeled as C in Table B.2
- Intermediate: sources with $0.75 \leq \mathcal{R} < 0.95$, labeled as I in Table B.2.
- Extended: sources with $\mathcal{R} < 0.75$, labeled as E in Table B.2.

Most sources of our sample are compact, but at the lowest frequency band (LOFAR data) a much higher fraction of the sources are extended (60% at 144 MHz, vs 11%, 17%, 11% and 11% at 1.5, 3, 5 and 10 GHz respectively).

Overall, only three targets show clear extended emission at most frequencies: J00418+4021, J12562+5652 and J17014+5149. J00418+4021 and J12562+5652 have faint diffuse emission, especially visible at lower frequencies, surrounding their bright core. The case of J17014+5149 is different: its radio emission resolves into two distinct point-like sources at high frequency.

We present the distribution of radio morphology detected across the various redshifts of our sources in Figure 2. Extended emission is detected even in our highest-redshift sources. At the highest redshift (0.75, J12075+1506), our highest resolution images resolve structures down to 2-3 kpc, which should be enough to resolve relativistic jets or SF.

3.3. Radio spectral index

Multi-frequency radio observations allow us to precisely measure the spectral index, helping us to understand the origin of the radio emission. We adopt $S_v \propto \nu^\alpha$, where α is the spectral index.

We measure the spectral index between bands such as:

$$\alpha_{\nu_1-\nu_2} = \frac{\log(S_2/S_1)}{\log(\nu_2/\nu_1)}, \quad (2)$$

where S_1 and S_2 are the flux densities at the observing frequencies ν_1 and ν_2 , respectively. To measure the global spectral index across the whole frequency range available, we fitted the fluxes across the bands using `NUMPY.POLYFIT` for sources with detection in at least three bands. Uncertainties in the spectral indices were calculated using standard propagation of errors. All the spectral indices are reported in Table B.4. We plot the spectrum of each source detected in at least three bands in Figure B.1. From the three sources identified with significant variability in VLASS observations, we note that the flux from J12562+5652 non-simultaneous observations at 144 MHz and 3 GHz fall outside of the fitted spectral slope.

For the few sources with extended emission at lower frequencies, the large mismatch in resolution with higher frequencies images prevented a spatially resolved analysis of the spectral index. In the case of J17014+5149, where two distinct point-like sources are resolved at C and X bands, we calculated the spectral indices of each point-like source. We used the CASA task `IMSMOOTH` to smooth the X-band image to the C-band beam (which has the lowest spatial resolution) and then apply the CASA task `IMREGRID` to regrid the X-band image using the C-band image as reference. We extracted fluxes from both point-like sources and obtained identical values (within the uncertainties) of $\alpha_{5-10} = -1.0 \pm 0.1$. This is consistent with the spectral index calculated from the integrated flux of the sources.

A common approach to characterize radio spectra is the use of radio color-color diagrams. We show the spectral indices $\alpha_{0.144-1.5}$ versus $\alpha_{1.5-3}$, $\alpha_{1.5-3}$ versus α_{3-5} and α_{3-5} versus α_{5-10} in Figure 3, top panels. To remove the impact of non-simultaneous observations as well as the missing LOFAR images and the non-detections from VLASS images, we also show a color-color diagram including only the L, C and X-band VLA observations: $\alpha_{1.5-5}$ versus α_{5-10} in Figure 3. We do not identify any sources with an ultra steep drop-off (see blue area in Figure B.1-right), indicative of relic emission, when significant cooling happened since the last AGN activity, leading to a spectrum with exceptional steepening ($\alpha < -2$) at high frequencies. This is consistent with [Fraix-Burnet et al. \(2017\)](#), where xA sources are interpreted as AGN in an early evolutionary stage.

We use these spectral indices to calculate the radio luminosity of the detected sources:

$$L_{1.4GHz} = 4\pi D_L^2 S_{1.4GHz} (1+z)^{-\alpha-1}, \quad (3)$$

where $L_{1.4GHz}$ is the radio luminosity (W Hz^{-1}) at 1.4 GHz, D_L is the luminosity distance (Mpc), calculated with Astropy using the redshifts from Table 1, α is the spectral index calculated by measuring the fitted spectral index, and $S_{1.4GHz}$ is the integrated radio flux density at 1.4 GHz extrapolated using the fitted spectral index. These luminosities are reported in Table B.4.

Radio-to-mid IR flux ratio is a useful tool to identify the source of radio emission since it differs significantly for jet-dominated AGN (i.e. blazars) and star-forming galaxies. We follow [Caccianiga et al. \(2015\)](#) and use the two point spectral index between 1.5GHz and 22 μm , defined as:

$$\alpha_{1.5}^{22} = -\frac{\log(S_{1.5}/S_{22})}{\log(1.5\text{GHz}/(c/22\mu\text{m}))}, \quad (4)$$

where S_{22} is the flux densities at 22 μm , as well as the $Q22$ parameter, defined as:

$$Q22 = \log(S_{22}/S_{1.5}). \quad (5)$$

Blazars, for which the radio emission is dominated by the relativistic jet, have steep $\alpha_{1.5}^{22} > 0.2$ indices, while star forming infrared galaxies have $\alpha_{1.5}^{22} < -0.25$, with SF as the main contributor to the radio emission [Caccianiga et al. \(2015\)](#). The distribution of radio-to-mid IR flux ratios of the detected sources in our sample is shown on Fig. 4: all sources have $\alpha_{1.5}^{22}$ below ~ -0.1 except two, J12091+5611 ($\alpha_{1.5}^{22} = 0.02$) and J14258+3946 ($\alpha_{1.5}^{22} = 0.16$). The distribution does not span a range as wide as in [Caccianiga et al. \(2015\)](#). Instead we find only a few objects with intermediate values: J12091+5611 ($\alpha_{1.5}^{22} = 0.02$), J12366+5630 ($\alpha_{1.5}^{22} = -0.14$) and J14475+3455 ($\alpha_{1.5}^{22} = -0.16$). For these sources, the radio emission most likely origin from a combination of jet and SF.

The flux densities at 22 μm measured for our sources and used to derived the $Q22$ parameter could be affected by the suite of broad emission bands from polycyclic aromatic hydrocarbons (PAHs) molecules. The PAH bands are tracers of star formation activity, and the 11.3 μm feature is believed to remain so even in the presence of an AGN ([Diamond-Stanic & Rieke 2012](#)). Considering the redshift of our sample, the $Q22$ parameter could be affected mainly by the relatively weak feature at $\approx 17\mu\text{m}$ ([Smith et al. 2007](#)). With a typical equivalent width in the observed frame of $\sim 0.5\text{\AA}$, it is expected to contribute only to slightly more than $\sim 10\%$ to the total flux in the S_{22} band. PAH features are also expected to be fainter in type-1 AGN, either because of dilution or destruction by the AGN radiation field ([Xie & Ho 2022](#)). A systematic analysis of the MIR properties of the present sample would be in order, considering the mixed nature of these sources, but is beyond the scope of the present work. However, we do not use $Q22$ as diagnostic of star formation, but rather as diagnostic for the presence of an excess radio emission that lowers $Q22$ and increases $\alpha_{1.5}^{22}$. We therefore classify the 2 sources that fall in the blazar domain (i.e. with $\alpha_{1.5}^{22} > 0$) as core/jet dominated.

3.4. Star formation estimates

We obtain star formation estimates from the IR and radio luminosity following [Ganci et al. \(2019\)](#). Using the starburst calibration derived by [Kennicutt \(1998\)](#), we estimate the SFR based on the IR luminosity with:

$$\text{SFR}_{60\mu\text{m}} \approx 4.5 \times 10^{-44} L_{60\mu\text{m}}, \quad (6)$$

where $\text{SFR}_{60\mu\text{m}}$ is in $M_{\odot}\text{yr}^{-1}$ and $L_{60\mu\text{m}}$ in erg/s is derived from 60 μm flux densities from IRAS and ISO data as:

$$L_{60\mu\text{m}} = 4\pi D_L^2 \nu S_{60\mu\text{m}} / K_{\text{FIR}}, \quad (7)$$

with K_{FIR} being the K correction in the FIR that we estimated as in equation 10 of [Ganci et al. \(2019\)](#). It is of order unity, varying within the range $\sim 1 - 1.4$. The SFR derived from 60 – 70 μm samples roughly the peak of the emission from warmer dust (50 - 60 K). Galaxies with hotter dust (e.g. very compact starbursts) will have a higher 60 μm /100 μm ratio than cooler, more quiescent disks. Conversely, cold cirrus tails will depress $L_{60\mu\text{m}}$ relative to the total FIR emission. We also considered $L(\text{FIR})$ from IRAS data at 60 μm and 100 μm ($L(\text{FIR})$ defined from a linear combination of the 60 μm and 100 μm fluxes according to [Helou et al. 1985](#), see Tab. B.3). $L(\text{FIR})$ is comparable to $L_{60\mu\text{m}}$, with some scatter associated with differences in the 100 μm /60 μm ratio ranging from ≈ 0.8 to 2. The different origin of the FIR emission at 60 μm and 100 μm make it preferable that the 60 μm scaling is used for comparison with radio emission, as it is expected to be more closely connected to recent star formation.

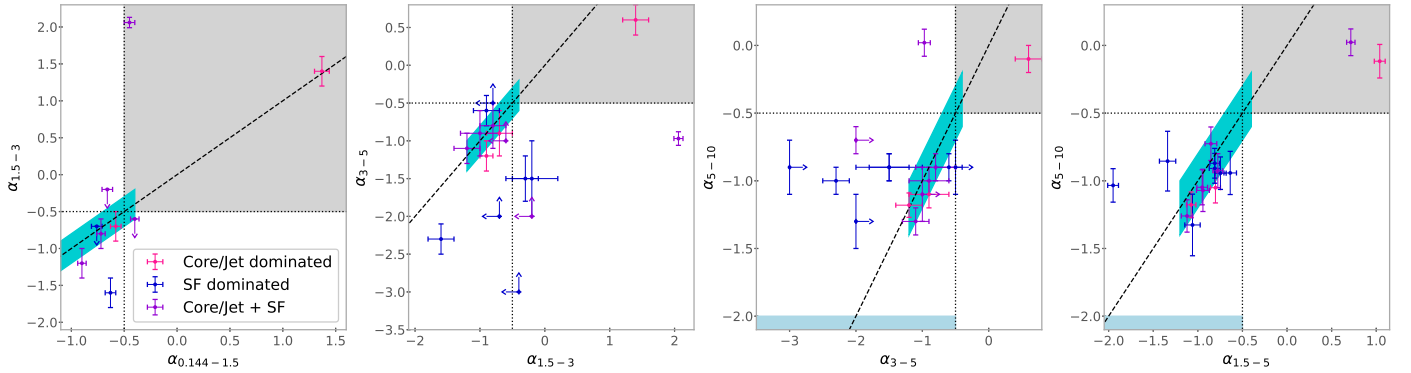


Fig. 3: The spectral indices $\alpha_{1.5-5}$ versus $\alpha_{0.144-1.5}$, α_{3-5} versus $\alpha_{1.5-3}$, α_{5-10} versus α_{3-5} and α_{5-10} versus $\alpha_{1.5-5}$. Markers are colored depending on the identified dominating mechanism behind the detected radio emission (Table 2). The dashed line is the 1 : 1 ratio line of equal slopes, while the horizontal and vertical dotted lines are $\alpha = -0.5$. The area showing flat or inverted spectra, which may be associated with a core-dominated jet or a corona, is filled in gray. The area with a spectral index $\alpha = -0.8 \pm 0.4$ with a scatter of 0.2, which may be related to SF, is filled in turquoise. The area showing very steep spectral slopes with $\alpha_{5-10} < -2$ in the right-hand panel, which may imply possible relic emission, is filled in blue.

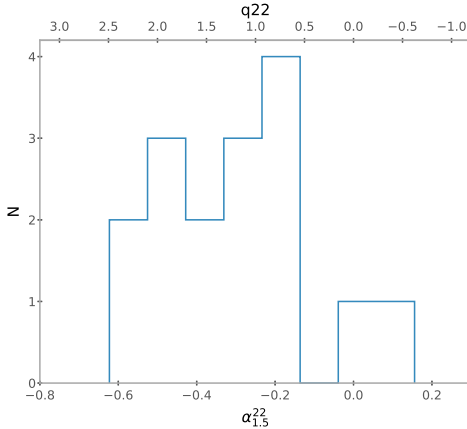


Fig. 4: Distribution of the two-point spectral index between radio (1.4 GHz) and mid-IR (22 μm). All sources have $\alpha_{1.5}^{22}$ below ~ -0.1 except J12091+5611 and J14258+3946.

However, for sources at $z \gtrsim 0.5$, the wavelength entering into the 60 μm band is $\lambda \lesssim 60/(1+z) \lesssim 40\mu\text{m}$. Even at 60 μm , there is a danger of contamination from the hot dust emission in the AGN torus (Mor & Netzer 2012; Netzer et al. 2016; Fuller et al. 2019). Nonetheless, the highest redshift sources for which there are usable FIR data are J15455+4846 and J17014+5149. In this case, the 60 μm scaling, and the $L(\text{FIR})$ yield SFR that are within a factor 2 from the SFR derived by ISO including the flux at 150 μm following the scaling by Stickel et al. (2000).

We compare the $L_{60\mu\text{m}}$ estimates with the radio pseudo-SFR for each object following eq. 22 of Molnár et al. (2021):

$$\log(p\text{SFR}_{\text{radio}}) = (0.823 \pm 0.009) \times \log(L_{1.4\text{GHz}}) - (17.5 \pm 0.2), \quad (8)$$

where $p\text{SFR}_{\text{radio}}$ is in $M_{\odot}\text{yr}^{-1}$ and $L_{1.4\text{GHz}}$ in W Hz^{-1} . These are displayed in Table B.4. $p\text{SFR}_{\text{radio}}$ assumes that all the radio emission detected is synchrotron emission associated with supernova remnants - which is incorrect for sources with an AGN-related contribution. Fig. 5 shows the FIR SFR estimate vs. radio pseudo-SFR for all sources radio-detected and with IRAS 60 μm data. For comparison we added star-forming galaxies (green), RQ quasars (blue) and RL quasars (red) from Bonzini et al. (2015), with their $p\text{SFR}_{\text{radio}}$ converted using eq. 22 of Molnár et al. (2021), with their $p\text{SFR}_{\text{radio}}$ converted using eq. 22 of Molnár et al. (2021).

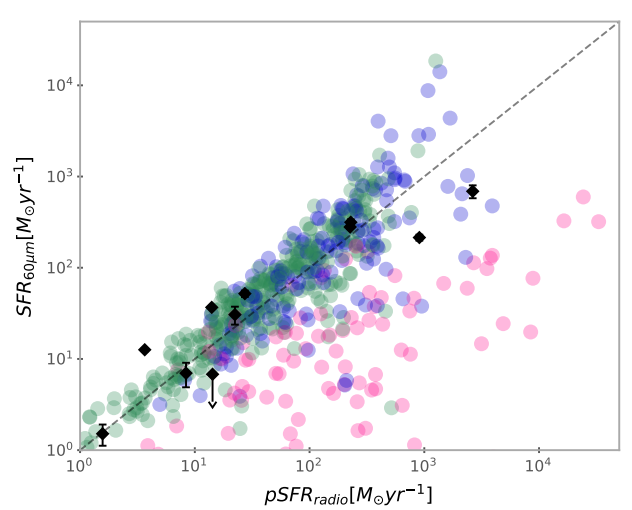


Fig. 5: SFR estimate based on FIR luminosity vs. radio pseudo-SFR for all sources radio-detected and with IRAS 60 μm data (black diamonds). Star-forming galaxies (green circles), RQ quasars (blue circles) and RL quasars (pink circles) are from Bonzini et al. (2015), with their $p\text{SFR}_{\text{radio}}$ converted using eq. 22 of Molnár et al. (2021). The dashed line is the 1 : 1 ratio line of equal SFR.

et al. (2021). All of the 10 sources with measured FIR SFR and radio pseudo-SFR more or less follow the 1 : 1 ratio line of equal SFR.

3.5. Classification of the dominating radio mechanism

The radio emission from the sources of our sample may be coming from a combination SF, AGN-driven winds/outflows, relativistic jets, and/or accretion disc coronal emission (Chen et al. 2022). For each source, we now intend to identify the dominating mechanisms based on the combination of several indicators, all compiled in Table 2. The calculated Kellermanns parameter R_k are shown for reference but were not used for the classifica-

Table 2: Indicators of the dominating mechanism behind the detected radio emission of the sources and overall classification

Object	$L_{1.4\text{GHz}}$	VLASS variability	Radio spectra	Radio morphology	FIR-radio correlation	$\alpha_{1.5}^{22}$	R_k	Overall Classification
J00418+4021	-	-	Linear/Curved	Extended	SF	SF	RL	SF dominated
J00457+0410	-	-	-	-	-	-	-	-
J00535+1241	-	-	Linear/Curved	C/I	SF	SF	RQ	SF dominated
J10255+5140	-	-	Linear/Curved	C/I	SF	SF	RQ	SF dominated
J11292-0424	-	-	Linear/Curved	C/I	SF	SF	RQ	SF dominated
J11420+6030	-	-	Linear/Curved	C/I	-	Combination	RQ	Core/Jet + SF
J12075+1506	Core/Jet	-	Linear/Curved	C/I	-	SF	RQ	Core/Jet + SF
J12091+5611	-	Core/Jet	Linear/Curved	C/I	-	Core/Jet	RL	Core/Jet dominated
J12366+5630	-	-	Linear/Curved	C/I	-	Combination	RL	Core/Jet + SF
J12562+5652	-	Core/Jet	Flat/Inverted	Extended	SF	SF	RL	Core/Jet + SF
J13012+5902	-	-	-	-	-	-	-	-
J14052+2555	-	-	Linear/Curved	C/I	SF	SF	RQ	SF dominated
J14063+2223	-	-	Linear/Curved	C/I	-	SF	RQ	SF dominated
J14170+4456	-	-	Linear/Curved	C/I	SF	SF	RQ	SF dominated
J14258+3946	Core/Jet	-	Flat/Inverted	C/I	-	Core/Jet	RL	Core/jet dominated
J14475+3455	Core/Jet	-	Linear/Curved	C/I	SF	Combination	RL	Core/Jet + SF
J15455+4846	-	Core/Jet	Linear/Curved	C/I	SF	SF	RL	Core/Jet + SF
J17014+5149	Core/Jet	-	Linear/Curved	Jets	SF	Combination	RL	Jet dominated

Notes. Column 1: Object coordinate name. Column 2: Sources with $\log L_{1.4\text{GHz}} > 31.6 \text{ erg s}^{-1} \text{ Hz}^{-1}$ certainly have an AGN-related contribution to their radio emission. Column 3: A variability index $V > 0.1$ (based on VLASS observations) indicate core/jet origin. Column 4: Shape of the radio spectra. Column 5: Particular morphology from radio observations - extended, compact or intermediate (C/I), or presence of jets. Column 6: Sources for which $p\text{SFR}_{\text{radio}} \simeq \text{SFR}_{60\mu\text{m}}$ are likely dominated by SF, while sources below the correlation are likely a combination. Column 7: Sources with $\alpha_{1.5}^{22} < -0.25$ are SF, those with $\alpha_{1.5}^{22} > 0$ are core/jet-dominated and the rest are combination of both. Column 8: For reference, the calculated Kellermanns parameter R_k (same as in last column of Table B.2). Column 9: Overall origin of the emission mechanism.

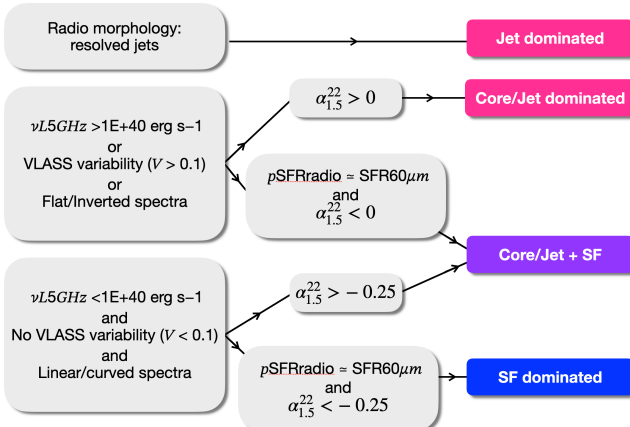


Fig. 6: Summary of the classification scheme used to identify the radio emission dominating mechanisms for each sources of our sample based on the combination of indicators compiled in Table 2.

tion. The classification scheme we decided to follow is shown on Figure 6, with details given below.

We first use the radio luminosity, which for starbursts typically do not exceed $\nu L_{\nu,\text{int}} = 1\text{E}+40 \text{ erg s}^{-1}$ (Sargsyan & Weedman 2009). We adopted the limit from Zamfir et al. (2008), $\log L_{1.4\text{GHz}} = 31.6 \text{ erg s}^{-1} \text{ Hz}^{-1}$. This indicates that the radio emission from at least 4 of our 18 sources must have an

AGN-related component (core or jet). Then, we note the three sources of our sample with significant radio variability at 3 GHz ($V > 0.1$), J12091+5611, J12562+5652 and J15455+4846, indicating a core or jet-related origin. We also consider the shape of the radio spectra obtained in section 3.3. SF produces a synchrotron spectrum with a $\alpha = -0.8 \pm 0.4$, no significant curvature from 1 – 10 GHz and a spectral turnover at around a few hundreds MHz. Radio emission from AGN jets has steeper spectral slopes with increasing frequencies, indicating the aging of the relativistic electron population due to inverse-Compton, synchrotron, ionization, or bremsstrahlung energy losses. Core-dominated jet or accretion disk corona produces optically thick synchrotron emission, characterized by a flat or inverted spectrum. From the 16 detected sources in at least three bands, 2 have flat or inverted spectra between 144 MHz (or 1.5 GHz) to 10 GHz: J12562+5652 and J14258+3946, with fitted spectral indices of 0.5 ± 0.3 and 1.0 ± 0.2 , respectively, both RL sources. J12562+5652 shows some extended emission (especially at 144 MHz), but, as it is the brightest source, the limited dynamical range reachable with the short exposure of the VLA observations might have prevented the detection of faint extended emission at higher frequencies (note the unusually high rms values from Table B.1 for this target). This explains why the flux density measured at 144 MHz appears way above the fitted spectral slope. J14258+3946 is the most luminous source of our sample and also has the highest $\alpha_{1.5}^{22} = 0.16$.

The non-simultaneity of the observations (LOFAR and VLASS) and the mismatch in resolution between frequencies

prevent us to clearly differentiate between SF vs jet origin for the rest of the sources with linear or curved spectrum.

J17014+5149 is the only source where we resolve two symmetrical radio jets. Indeed, the two distinct point-like sources resolved at higher frequencies have identical (within the uncertainties) $\alpha_{5-10} = -1.0 \pm 0.1$. It also has the second highest radio luminosity of all our sample. Due to this morphology, we directly classify it as jet-dominated. For the rest of the sources, their morphologies or just the presence or lack-of extended emission do not allow us to constrain more the classification.

While correlation is not causation, we consider that the 10 sources having $p\text{SFR}_{\text{radio}} \simeq \text{SFR}_{60\mu\text{m}}$ are likely to have their radio emission from SF origin (see Figure 5). None of these sources are located below the correlation, indicating that the entire detected radio emission can be resulting from SF. In addition to this criteria, we consider the two-point spectral index between radio and mid-IR (see Figure 4). We divided sources with $\alpha_{1.5}^{22} < -0.25$, typical of star forming infrared galaxies, from those with $\alpha_{1.5}^{22} > 0$ (more typical of core or jets), while for the rest of the sources, the radio emission likely origin from a combination of the AGN and SF. Only one source, J12075+1506, for which no IR data is available, cannot be classified following exactly the classification scheme from Figure 6. However, since it has $\log L_{1.4\text{ GHz}} > 31.6 \text{ erg s}^{-1} \text{ Hz}^{-1}$ and $\alpha_{1.5}^{22} < -0.25$, the origin of its emission has been interpreted as a combination of the AGN and SF.

Overall, we find that 7 of our 18 targets are likely to have their radio emission dominantly coming from SF, and 6 from a combination of SF and AGN-related mechanism. Only three sources (all RL) indicate a core or jetted AGN only origin for the detected radio emission. Among the 8 RL sources, one is classified as SF dominated and four as a combination of SF and AGN-related mechanism.

3.6. Bremsstrahlung radio emission

Free-free (Bremsstrahlung) emission arises from hot, ionized gas. The mechanism itself operates independently of bulk motion, while a BLR or a NLR wind could contribute to or enhance such emission particularly by providing a more extended or structured ionized medium. The vast majority of super-Eddington sources in our sample exhibit evidence of $[\text{OIII}]\lambda\lambda 4959,5007$ outflows (see the results of the multicomponent nonlinear analysis of the $[\text{OIII}]\lambda\lambda 4959,5007$ line and estimation of wind parameter in Appendix C), which in some cases are powerful enough to dominate the line emission. For sources with high Eddington ratios, free-free emission associated with a wind is a plausible contribution to their radio output (Blundell & Kuncic 2007; Chen et al. 2024).

As shown in the previous sections (Sect. 3.3), in our sample the radio spectral indices are in general not consistent with sole optically thin or thick Bremsstrahlung emission (Baskin & Laor 2021) nor with emission from a corona. The energetics of the $[\text{OIII}]\lambda 5007$ outflows also disfavors Bremsstrahlung emission as the origin for the radio power.

The mass of the gas emitting the $[\text{OIII}]\lambda 5007$ lines can be computed by using a conversion between line luminosity and gas mass (Cano-Díaz et al. 2012; Carniani et al. 2015; Marziani et al. 2016b, 2017; Fiore et al. 2017):

$$M_{[\text{OIII}]} \sim 1 \cdot 10^6 L_{44} \left(\frac{Z}{5Z_\odot} \right)^{-1} n_4^{-1} M_\odot \quad (9)$$

where the line luminosity is expressed in units of $10^{44} \text{ erg s}^{-1}$, the metallicity is scaled to five times solar, and the density is normalized to 10^4 cm^{-3} . Given the free-free emissivity j_{ff} (Rybicki & Lightman 1979), the radio power expected from the emitting gas is:

$$P_{\nu, [\text{OIII}]} \sim \frac{M_{[\text{OIII}]} j_{\text{ff}}}{n \mu m_p} \sim 2.9 \cdot 10^{29} \bar{g}_{10} T_{\text{e},10000}^{-1/2} Z_5^{-1} \cdot n_4 L_{[\text{OIII}],44} \text{ erg s}^{-1} \text{ Hz}^{-1} \quad (10)$$

where \bar{g}_{10} is value for the average Gaunt factor normalized to 10 (Van Hoof et al. 2014, 2015; Chluba et al. 2020). The typical density of the spatially resolved NLR is $n \gtrsim 10^3 \text{ cm}^{-3}$ (Singha et al. 2022, c.f. Kakkad et al. 2018); an upper limit could be provided density of the innermost part of the NLR of NGC 5548 has been found to be $n \sim 10^5 \text{ cm}^{-3}$ (Peterson et al. 2013). We therefore scaled the equation for the radio-power to $n \sim 10^4 \text{ cm}^{-3}$. If so, the observed median $[\text{OIII}]\lambda 5007$ luminosity of $\sim 10^{42} \text{ erg s}^{-1}$ (Appendix C) is not sufficient to explain the observed radio power, especially if $L_{1.4\text{ GHz} \gtrsim 10^{31}} \text{ erg s}^{-1} \text{ Hz}^{-1}$. In the case of a compact NLR (Zamanov et al. 2002), however, a higher density $\sim 10^5 \text{ cm}^{-3}$ of the $[\text{OIII}]\lambda 5007$ emitting region could account for powers comparable to $L_{1.4\text{ GHz}} \sim 10^{29} \text{ erg s}^{-1} \text{ Hz}^{-1}$.

3.7. Correlation analysis

3.7.1. Accretion parameters vs radio spectral indices

Laor et al. (2019) compared the radio spectral index of a sample of 25 RQ PalomarGreen (PG) quasars with the Eddington ratio, the FWHM of the $\text{H}\beta$ line, the flux ratio R_{FeII} and M_{BH} . They found that radio quiet and radio loud quasars were showing different trends. The radio spectral indices of the radio quiet quasars in their sample correlate with the FWHM of the $\text{H}\beta$ line as well as with the Eddington ratio: high Eddington ratio sources have steeper radio spectrum (indicative of an extended optically thin synchrotron source, i.e. possibly a weak jet or wind component) while lower Eddington ratio sources have flatter radio spectrum (indicative of a compact optically thick synchrotron source, i.e. compact core, possibly a weak jet base or an accretion disc corona). Radio loud quasars do not show such a correlation but their radio spectral indices correlate with M_{BH} : most quasars with $M_{\text{BH}} > 10^9 M_\odot$ have a steeper (< -0.5) spectral indices (radio is dominated by the extended lobe emission) while $M_{\text{BH}} < 10^9 M_\odot$ quasars have spectral indices > -0.5 , and their radio emission is unresolved.

We compare these results with our sample in Fig. 7. The distribution of our sources mainly overlap the radio quiet quasars from Laor et al. (2019). Indeed, most of the xA data points (those classified SF-dominated and Core/Jet+SF, all with $\alpha_{5-10} \lesssim -0.5$) are consistent with the high L/L_{Edd} branch of Laor et al. (2019). A single source in our sample (J12562+5652 \equiv Mark 231) is special in that it has an inverted spectrum ($\alpha_{5-10} > 0$); this object may correspond more to the RL regime of Laor et al. (2019). An important difference is that two core-jet dominated objects show $R_{\text{FeII}} > 1$, while all RL sources of Laor et al. (2019) show $R_{\text{FeII}} \lesssim 0.5$, and that those core-jet dominated sources in our sample have Eddington ratio close to 1.

3.7.2. Correlation of radio, IR and optical data

The data for the xA sources allow for a correlation analysis between radio, IR, and optical spectral properties. Fig. C.2 shows

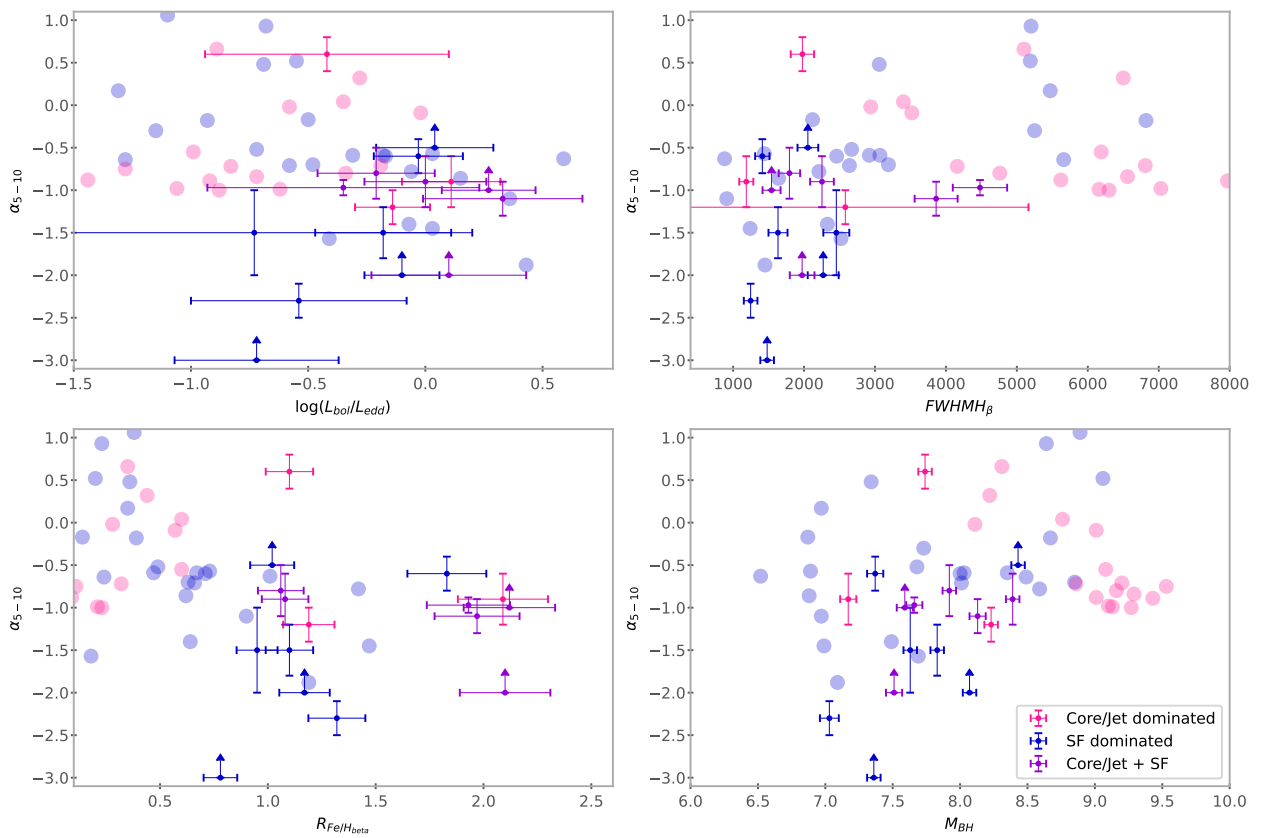


Fig. 7: The spectral index α_{5-10} versus the Eddington ratio, the FWHM of the $H\beta$ line (in km/s), the flux ratio R_{FeII} and M_{BH} . Markers are colored depending on the identified dominating mechanism behind the detected radio emission (Table 2). Blue (pink) filled circles represents the radio quiet (loud) quasars respectively from Laor et al. (2019).

the results for most parameters measured in the present papers (from Tables B.4, C.1, C.2 and C.4, or computed as explained in the previous sections). Apart from some predictable correlations (for example, M_{BH} and L/L_{Edd} with luminosity), correlations between R_{FeII} and L/L_{Edd} have been found or predicted in several past works (Marziani et al. 2001; Sun & Shen 2015; Du et al. 2016; Marziani et al. 2025, and references therein). This correlation is not especially strong since almost all sources of the sample are strong FeII-emitters, which implies that all have low equivalent width W albeit broad $[\text{OIII}]\lambda\lambda4959,5007$ and blueward asymmetries in both $H\beta$ and $[\text{OIII}]\lambda5007$. The anti-correlation between $[\text{OIII}]\lambda5007$ BLUE peak shift and its FWHM is typical of compact, wind dominated narrow-line regions (NLR, Zamanov et al. 2002; Marziani et al. 2016b; Coatman et al. 2016; Deconto-Machado et al. 2023). An important result is the lack of a strong correlation ($r_p \lesssim 0.3$) between radio-power and $[\text{OIII}]\lambda5007$ and $H\beta$ mass outflow rate $\dot{M} H\beta$.

3.7.3. Principal component analysis

The Eigenvector 1 of quasars (E1) has been retrieved in samples where the R_{FeII} range is $\approx 0 - 2$ (Boroson & Green 1992), while in the present sample, the median value is $R_{FeII} \approx 1.19$, with a 1st quartile at $R_{FeII} \approx 1.09$, and only one object (J10255+5140) with $R_{FeII} \approx 0.8$. In lieu of the correlation between R_{FeII} and L/L_{Edd} (Du et al. 2016; Panda et al. 2019), and of L/L_{Edd} varying little for $R_{FeII} \gtrsim 1$ (Marziani et al. 2025), we cannot expect to detect the Eigenvector 1 in our sample. The PCA applied to our sample reveals only 1 eigenvector with a clear physical meaning. Fig. 8

shows the projection of the targets, and the loads of each vector along principal component 1 (PC1). The PC1 carries $\approx 34\%$ of the sample variance (a bit more than the original E1, but it is associated with trends due to luminosity, i.e., with the original E2 of Boroson & Green (1992). The left panel of Fig. 8 shows the sources of our sample aligned along the PC1: the least and the most luminous ones are located at the opposite ends of the vector.

4. Discussion

4.1. Significance of the high R_{FeII} and jetted super-Eddington candidates

In our sample, we have found three sources (J12091+5611, J14258+3946 and J17014+5149, all RL) for which their radio emission is dominantly coming from a core or jetted AGN. As shown by Fig. 1, the interpretation of the prevalence of radio-detected and genuinely jetted sources—starting from an optically selected sample—depends on the location along the MS. A rigorous assessment of the incidence of jetted sources would require homogeneous datasets and well-defined parent samples that are not readily available. As a pragmatic proxy, one may consider NLSy1s, even though only a minority of them satisfy the condition $R_{FeII} \gtrsim 1$. While the most powerful radio sources belong to the B spectral types, a population of lower-power, yet jetted, objects has been uncovered among NLSy1s (Komossa et al. 2006; Foschini et al. 2015; Foschini 2020). About 7 per cent of NLSy1s are radio loud, with an even smaller fraction (~ 2.5 per cent) reaching very high radio loudness ($R_K > 100$)

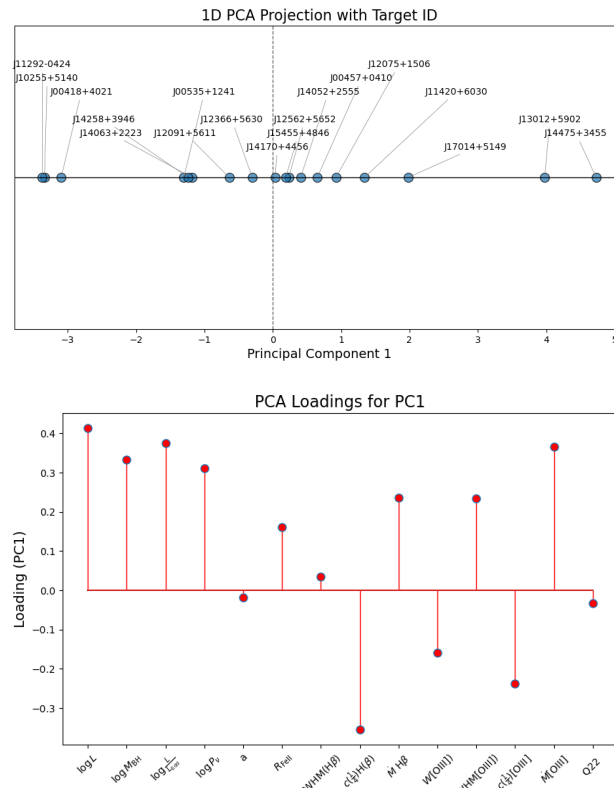


Fig. 8: Results of the PCA analysis: top, 1D projection of sources along the PC1; bottom, vector loading along the PC1.

(Orienti et al. 2015). Sources detected in the γ -ray domain are far fewer: $\lesssim 30$ are currently known (Foschini 2020; Foschini et al. 2022; Barba et al. 2025). Moreover, objects with reliable measurements (i.e., high S/N optical spectra) that simultaneously meet $R_{\text{FeII}} \gtrsim 1$ and are demonstrably jetted—as indicated by a high radio-loudness parameter, $\log R_K \gtrsim 1.8$ (Zamfir et al. 2008)—are extremely rare. A search in the recent catalog by Paliya et al. (2023) returns only a handful of candidates among $\sim 28,000$ NLSy1s. Only a handful of the γ -ray emitters would be classified as xA. A couple of additional jetted candidates is reported in the sample of Garnica et al. (2025), defined by $R_{\text{FeII}} \gtrsim 0.9$. In addition, some observational studies are reporting compact or jet-like radio emission in high-Eddington systems among eROSITA detected X-ray quasars (e.g., Khorunzhev et al. 2021; Wolf et al. 2021; Obuchi et al. 2025).

Super-Eddington accretors with relativistic ejections imply that thick, wind-dominated accretion flows can still generate and sustain magnetically driven, collimated jets. Coexistence is physically expected in a magnetically-arrested disk (MAD) regime because super-Eddington disks are geometrically thick and tend to create a low-density polar funnel while simultaneously launching a wide-angle wind from the disk surface (McKinney et al. 2015; Yang et al. 2023). The main threat to a highly relativistic jet is mass loading (baryons and radiation) in/near the funnel, which can reduce jet magnetization and terminal Lorentz factor (McKinney et al. 2015). The identification of jetted super-Eddington candidates is therefore of special relevance for a full understanding of the accretion process, and the sources identified in the present work should be considered for dedicated studies.

4.2. High-rate accretion and star formation

The analysis presented in the previous sections indicates that SF is among the emission mechanisms responsible for the radio emission of many sources of our sample. Indeed, we find that most have a radio spectral index corresponding with either SF or optically thin jet emission, but when considering the correlation between IR and radio properties, we determine a high prevalence of systems that have composite origin, or that are even SF dominated, showing the importance of a multi-wavelength analysis based on several indicators.

We selected our sample on the basis on an optical selection criterion $R_{\text{FeII}} \gtrsim 1$ which isolates spectral type A3/A4 in the 4DE1 formalism (Sulentic et al. 2000b). This selection is independent of radio properties, avoiding any explicit bias toward radio-loud or radio-quiet AGN. Sources in the A3/A4 bins are generally interpreted as radiating at high Eddington ratios, a key driver of Eigenvector 1, and are known to show strong FeII emission, narrow Balmer lines, and weak but semi-broad all hallmarks of high accretion states – cognate to the coexistence of a virialized low-ionization BLR coexisting with an outflowing, mildly ionized system involving both broad and narrow lines (Collin-Souffrin & Lasota 1988; Elvis 2000; Marziani et al. 2010). Our high Eddington ratio sample reveals a high prevalence of systems that have composite radio or are even SF dominated. Within this framework, our results confirm previous SDSS-based statistical findings: a significant fraction of the high- R_{FeII} sources exhibit either composite radio emission or emission dominated by star formation (Bonzini et al. 2015; Ganci et al. 2019). Consistent results were also found by the analysis of NLSy1 samples (Sani et al. 2010; Caccianiga et al. 2015), as such sample involve a large fraction of highly accreting sources (even if not all NLSy1s are highly accreting sources, Marziani et al. 2018). The evidence supports the view that in the high Eddington ratio regime, the prevalence of powerful relativistic jets diminishes, while other forms of radio emissions such as compact or diffuse low-power radio structures associated with winds, disk instabilities, or star-forming activity become more common. The relative paucity of high radio power sources for low M_{BH} AGN may ultimately support a mechanism in which the radio power scales with the M_{BH} , such as extraction of energy from a spinning black hole threaded by magnetic fields (Blandford & Znajek 1977; Foschini 2014; Foschini et al. 2024).

The E1 main sequence, even as it is observed at low redshifts, allows for an evolutionary interpretation (Fraix-Burnet et al. 2017): from the highly-accreting low mass AGN, to the evolved, massive black holes accreting at low rates down to minimum needed to sustain radiative-efficient accretion (Giustini & Proga 2019). Figure 7 of Yue et al. (2025) presents cumulative M_{BH} distributions for AGN whose low-frequency radio is AGN- and star formation-dominated, broken down across a grid in luminosity and redshift. A key result is the consistent offset: AGN-dominated quasars have systematically higher black hole masses than SF-dominated ones, across all bins. In the context of a sample selected via high $R_{\text{FeII}} \gtrsim 1$, which maps to spectral types A3/A4 and thus to high Eddington ratio sources, the results of Yue et al. (2025) are especially informative: sources with lower M_{BH} are expected to have relatively higher L/L_{Edd} at fixed luminosity due to the inverse relation between L/L_{Edd} and M_{BH} for a given bolometric output. The star-formation-dominated quasars likely corresponding to high- L/L_{Edd} systems in our sample tend to be less massive than their jetted counterparts. This behavior consistently extends from low- z to beyond the cosmic noon, and suggests a common pattern in the evolution of quasars and

growth of their black holes, in which star formation, possibly associated with an enhancement of the amount of gas available in proximity of the active nucleus induced by a merging, is co-existing in the early phases of the growth of the black hole. As the quasars evolves from xA to the extreme population B, the black hole mass increases and the circum-nuclear stellar system evolves, with some stars following accretion-modified stellar evolution pattern (e.g., Wang et al. 2010, 2009; Cantiello et al. 2021; Fabj & Samsing 2024). In the end, the most massive black holes are expected to be surrounded by a stellar graveyard (Marziani et al. 2025).

5. Conclusions

We present new VLA observations at L, C and X-band of a sample of 18 quasars accreting at very high rates, which we combine with LoTSS and VLASS observations. We identify the dominating mechanism behind the detected radio emission of these sources based on a combination of several indicators : radio variability, luminosity, morphology, radio spectral properties and radio-to-mid IR flux ratio. We find that 7 of our 18 targets are likely to have their radio emission dominantly coming from SF, and 6 from a combination of SF and AGN-related mechanism. Only three sources indicate a core or jetted AGN only origin for the detected radio emission. This is consistent with previous studies and suggests that, in the highEddington-ratio regime, radio emission is more commonly associated with lower-power structures related to star formation than with relativistic jets. We discuss how this fits into a common evolutionary pattern of quasars, in which star formation is coexisting in the early phases of the growth of the black hole. A PCA analysis confirms the tendency toward homogeneous properties of the sample sources consistent with a common spectral type with the first eigenvector being associated with luminosity-dependent effects.

We add to the analysis a multi-component nonlinear decomposition of H β and [OIII] $\lambda\lambda 4959,5007$ lines, from which we derive estimation of accretion and wind parameters. While these sources are mostly candidate super-Eddington quasars, their NLR and BLR winds only produce the modest feedback, especially at low-luminosity. We also estimate the Bremsstrahlung emission associated with the condition needed for formation of the [OIII] $\lambda\lambda 4959,5007$ lines in the context of photoionization from the active nucleus, but find no clear evidence of its contribution to the total radio power in the present sample.

The upcoming Square Kilometre Array Observatory, with its unparalleled sensitivity and angular resolution, will allow to conduct similar studies and probe the evolution of these objects at much earlier times (e.g. Latif et al. 2024).

Acknowledgements. MLGM and LVM acknowledge financial support from the grant CEX2021-001131-S funded by MICIU/AEI/10.13039/501100011033, from the grant PID2021-123930OB-C21 funded by MICIU/AEI/10.13039/501100011033 and by ERDF/EU. MLGM acknowledges financial support from NSERC via the Discovery grant program and the Canada Research Chair program. AdO and PM acknowledge financial support from the Spanish MCIU through project PID2022-140871NB-C21 by ERDF A way of making Europe, and from the Severo Ochoa grant CEX2021-515001131-S funded by MCIN/AEI/10.13039/501100011033. LOFAR is the Low Frequency Array designed and constructed by ASTRON. It has observing, data processing, and data storage facilities in several countries, which are owned by various parties (each with their own funding sources), and which are collectively operated by the ILT foundation under a joint scientific policy. The ILT resources have benefited from the following recent major funding sources: CNRS-INSU, Observatoire de Paris and Université d'Orléans, France; BMBF, MIWF-NRW, MPG, Germany; Science Foundation Ireland (SFI), Department of Business, Enterprise and Innovation (DBEI), Ireland; NWO, The Netherlands; The Science and Technology Facilities Council, UK; Ministry of Science and Higher Education, Poland; The Istituto Nazionale di Astrofisica

(INAF), Italy. This research has made use of the NASA/IPAC Extragalactic Database (NED), which is operated by the Jet Propulsion Laboratory, California Institute of Technology, under contract with the National Aeronautics and Space Administration. This research has made use of the NASA/IPAC Infrared Science Archive, which is funded by the National Aeronautics and Space Administration and operated by the California Institute of Technology.

References

Aller, M. F., Aller, H. D., & Hughes, P. A. 1992, ApJ, 399, 16, aDS Bibcode: 1992ApJ...399..16A

Azzalini, A. 1985, Scand. J. Stat., 12, 171

Barba, B. D., Foschini, L., Berton, M., et al. 2025, Revised optical classification of a sample of gamma-ray emitting AGN with GTC and VLT, version Number: 1

Baskin, A. & Laor, A. 2021, MNRAS, 508, 680

Belladitta, S., Moretti, A., Caccianiga, A., et al. 2019, A&A, 629, A68

Bentz, M. C., Peterson, B. M., Netzer, H., Pogge, R. W., & Vestergaard, M. 2009, ApJ, 697, 160

Berton, M., Congiu, E., Järvelä, E., et al. 2018, A&A, 614, A87

Berton, M., Foschini, L., Ciroi, S., et al. 2016, A&A, 591, A88

Berton, M. & Järvelä, E. 2021, Universe, 7, 188, number: 6

Berton, M., Järvelä, E., Crepaldi, L., et al. 2020, A&A, 636, A64

Bischetti, M., Piconcelli, E., Vietri, G., et al. 2017, A&A, 598, A122

Blandford, R. D. & Znajek, R. L. 1977, MNRAS, 179, 433, aDS Bibcode: 1977MNRAS.179..433B

Blundell, K. M. & Kuncic, Z. 2007, ApJ, 668, L103

Bonzini, M., Mainieri, V., Padovani, P., et al. 2015, MNRAS, 453, 1079, aDS Bibcode: 2015MNRAS.453.1079B

Boroson, T. A. & Green, R. F. 1992, ApJS, 80, 109, aDS Bibcode: 1992ApJS...80..109B

Caccianiga, A., Antón, S., Ballo, L., et al. 2015, MNRAS, 451, 1795

Cano-Díaz, M., Maiolino, R., Marconi, A., et al. 2012, A&A, 537, L8

Cantiello, M., Jermyn, A. S., & Lin, D. N. C. 2021, ApJ, 910, 94

Carniani, S., Marconi, A., Maiolino, R., et al. 2015, A&A, 580, A102

CASA Team, Bean, B., Bhatnagar, S., et al. 2022, PASP, 134, 114501, aDS Bibcode: 2022PASP..134k4501C

Chen, S., Laor, A., Behar, E., et al. 2024, ApJ, 975, 35

Chen, S., Stevens, J. B., Edwards, P. G., et al. 2022, MNRAS, 512, 471, aDS Bibcode: 2022MNRAS.512..471C

Chluba, J., Ravenni, A., & Bolliet, B. 2020, MNRAS, 492, 177

Coatman, L., Hewett, P. C., Banerji, M., & Richards, G. T. 2016, MNRAS, 461, 647

Collin-Souffrin, S. & Lasota, J.-P. 1988, PASP, 100, 1041, aDS Bibcode: 1988PASP..100.1041C

Condon, J. J. 1989, ApJ, 338, 13

Condon, J. J., Huang, Z.-P., Yin, Q. F., & Thuan, T. X. 1991, ApJ, 378, 65

Cornwell, T. J. 2008, IEEE J. Sel. Topics Signal Process., 2, 793

Cornwell, T. J., Golap, K., & Bhatnagar, S. 2008, IEEE J. Sel. Topics Signal Process., 2, 647

Cracco, V., Ciroi, S., Berton, M., et al. 2016, MNRAS, 462, 1256

Crepaldi, L., Berton, M., Dalla Barba, B., et al. 2025, A&A, 696, A74

Cresci, G., Mainieri, V., Brusa, M., et al. 2015, ApJ, 799, 82

Czerny, B., Beaton, R., Bejger, M., et al. 2018, Space Sci. Rev., 214, 32

Decarli, R., Walter, F., Venemans, B. P., et al. 2017, Nat, 545, 457

Deconto-Machado, A., Del Olmo, A., & Marziani, P. 2024, A&A, 691, A15

Deconto-Machado, A., Del Olmo Orozco, A., Marziani, P., Perea, J., & Stirpe, G. M. 2023, A&A, 669, A83

Di Matteo, T., Springel, V., & Hernquist, L. 2005, Nat, 433, 604

Diamond-Stanic, A. M. & Rieke, G. H. 2012, ApJ, 746, 168, aDS Bibcode: 2012ApJ...746..168D

Du, P. & Wang, J.-M. 2019, ApJ, 886, 42

Du, P., Wang, J.-M., Hu, C., et al. 2016, ApJ, 818, L14

DOnofrio, M., Marziani, P., Chiosi, C., & Negrete, C. A. 2024, Universe, 10, 254, number: 6

Elvis, M. 2000, ApJ, 545, 63

Fabj, G. & Samsing, J. 2024, MNRAS, 535, 3630

Ferland, G. J., Done, C., Jin, C., Landt, H., & Ward, M. J. 2020, MNRAS, 494, 5917

Fiore, F., Feruglio, C., Shankar, F., et al. 2017, A&A, 601, A143

Foschini, L. 2014, Int. J. Mod. Phys. Conf. Ser., 28, 1460188

Foschini, L. 2020, Universe, 6, 136

Foschini, L., Barba, B. D., Tornikoski, M., et al. 2024, Universe, 10

Foschini, L., Berton, M., Caccianiga, A., et al. 2015, A&A, 575, A13

Foschini, L., Lister, M. L., Andernach, H., et al. 2022, Universe, 8, 587

Fraix-Burnet, D., D'Onofrio, M., & Marziani, P. 2017, Front. Astron. Space Sci., 4

Fuller, L., Lopez-Rodriguez, E., Packham, C., et al. 2019, MNRAS, 483, 3404

Ganci, V., Marziani, P., DONOFRIO, M., et al. 2019, *A&A*, 630, A110

Garnica, K., Dultzin, D., Marziani, P., & Panda, S. 2025, The spectral energy distribution of extreme population A quasars, arXiv:2505.22912 [astro-ph]

Giustini, M. & Proga, D. 2019, *A&A*, 630, A94

Greene, J. E. & Ho, L. C. 2005, *ApJ*, 630, 122

Halpern, J. P. & Oke, J. B. 1987, *ApJ*, 312, 91, aDS Bibcode: 1987ApJ...312..91H

Harrison, C. M., Alexander, D. M., Mullaney, J. R., & Swinbank, A. M. 2014, *MNRAS*, 441, 3306

Heinz, S. & Sunyaev, R. A. 2003, *MNRAS*, 343, L59

Helou, G., Soifer, B. T., & Rowan-Robinson, M. 1985, *ApJ*, 298, L7

Ishibashi, W. & Fabian, A. C. 2012, *MNRAS*, 427, 2998

Jarrett, T. H., Cohen, M., Masci, F., et al. 2011, *ApJ*, 735, 112, aDS Bibcode: 2011ApJ...735..112J

Jarvis, M. J. & McLure, R. J. 2006, *MNRAS*, 369, 182

Järvelä, E., Berton, M., & Crepaldi, L. 2021, *Front. Astron. Space Sci.*, 8

Järvelä, E., Dahale, R., Crepaldi, L., et al. 2022, *A&A*, 658, A12

Kakkad, D., Groves, B., Dopita, M., et al. 2018, *A&A*, 618, A6

Kakkad, D., Mainieri, V., Vietri, G., et al. 2020, *A&A*, 642, A147

Kakkad, D., Sani, E., Rojas, A. F., et al. 2022, *MNRAS*, 511, 2105

Kellermann, K. I., Sramek, R., Schmidt, M., Shaffer, D. B., & Green, R. 1989, *AJ*, 98, 1195

Kennicutt, R. C. 1998, *ARA&A*, 36, 189

Kessler, M. F., Steinz, J. A., Anderegg, M. E., et al. 1996, *A&A*, 315, L27, aDS Bibcode: 1996A&A...315L..27K

Khorunzhev, G. A., Meshcheryakov, A. V., Medvedev, P. S., et al. 2021, *Astron. Lett.*, 47, 123

King, A. & Muldrew, S. I. 2016, *MNRAS*, 455, 1211

King, A. & Pounds, K. 2015, *ARA&A*, 53, 115

Komossa, S., Voges, W., Xu, D., et al. 2006, *AJ*, 132, 531

Kunert-Bajraszewska, M., Krauze, A., Kimball, A. E., et al. 2025, *ApJS*, 277, 50

Lacy, M., Baum, S. A., Chandler, C. J., et al. 2020, *PASP*, 132, 035001

Laha, S., Reynolds, C. S., Reeves, J., et al. 2020, *Nat Astron*, 5, 13

Laor, A., Baldi, R. D., & Behar, E. 2019, *MNRAS*, 482, 5513

Latif, M. A., Whalen, D. J., & Mezcua, M. 2024, *Mon Not R Astron Soc Lett*, 527, L37

Leighly, K. M. & Moore, J. R. 2004, *ApJ*, 611, 107

Liska, M. T. P., Musoke, G., Tchekhovskoy, A., Porth, O., & Beloborodov, A. M. 2022, *ApJL*, 935, L1

Lähteenmäki, A., Järvelä, E., Ramakrishnan, V., et al. 2018, *A&A*, 614, L1

Mancuso, C., Lapi, A., Prandoni, I., et al. 2017, *ApJ*, 842, 95

Martínez-Aldama, M. L., Del Olmo, A., Marziani, P., et al. 2018, *A&A*, 618, A179

MartínezAldama, M. L., Zajaek, M., Czerny, B., & Panda, S. 2020, *ApJ*, 903, 86

Marziani, P., Berton, M., Panda, S., & Bon, E. 2021, *Universe*, 7, 484, number: 12

Marziani, P., Dultzin, D., Sulentic, J. W., et al. 2018, *Front. Astron. Space Sci.*, 5, 6

Marziani, P., Garnica Luna, K., Floris, A., et al. 2025, *Universe*, 11, 69

Marziani, P., MartínezCarballo, M. A., Sulentic, J. W., et al. 2016a, *Ap&SS*, 361, 29

Marziani, P., Negrete, C. A., Dultzin, D., et al. 2017, *Front. Astron. Space Sci.*, 4

Marziani, P., Olmo, A. d., Negrete, C. A., et al. 2022, *ApJS*, 261, 30

Marziani, P. & Sulentic, J. W. 2014, *MNRAS*, 442, 1211

Marziani, P., Sulentic, J. W., Negrete, C. A., et al. 2010, *MNRAS*, 409, 1033

Marziani, P., Sulentic, J. W., Plauchu-Frayn, I., & Olmo, A. d. 2013, *A&A*, 555, A89

Marziani, P., Sulentic, J. W., Stirpe, G. M., et al. 2016b, *Ap&SS*, 361, 3

Marziani, P., Sulentic, J. W., Zamanov, R., et al. 2003, *ApJS*, 145, 199

Marziani, P., Sulentic, J. W., Zwitter, T., Dultzin-Hacyan, D., & Calvani, M. 2001, *ApJ*, 558, 553

Mathur, S. 2000, *MNRAS*, 314, L17

McKinney, J. C., Chluba, J., Wielgus, M., Narayan, R., & Sadowski, A. 2017, *MNRAS*, 467, 2241

McKinney, J. C., Dai, L., & Avara, M. J. 2015, *MNRAS Letter*, 454, L6

Mejia-Restrepo, J. E., Lira, P., Netzer, H., Trakhtenbrot, B., & Capellupo, D. M. 2018, *Nat Astron*, 2, 63

Mineshige, S., Kawaguchi, T., Takeuchi, M., & Hayashida, K. 2000, *PASJ*, 52, 499

Molnár, D. C., Sargent, M. T., Leslie, S., et al. 2021, *MNRAS*, 504, 118, aDS Bibcode: 2021MNRAS.504..118M

Mor, R. & Netzer, H. 2012, *MNRAS*, 420, 526

Murakami, H., Baba, H., Barthel, P., et al. 2007, *PASJ*, 59, S369

Nardini, E., Lusso, E., Risaliti, G., et al. 2019, *A&A*, 632, A109

Negrete, C. A., Dultzin, D., Marziani, P., et al. 2018, *A&A*, 620, A118

Negrete, C. A., Dultzin, D., Marziani, P., & Sulentic, J. W. 2012, *ApJ*, 757, 62

Netzer, H. 2013, The Physics and Evolution of Active Galactic Nuclei, publication Title: The Physics and Evolution of Active Galactic Nuclei aDS Bibcode: 2013peag.book.....N

Netzer, H. 2019, *MNRAS*, 488, 5185

Netzer, H., Lani, C., Nordon, R., et al. 2016, *ApJ*, 819, 123

Netzer, H. & Marziani, P. 2010, *ApJ*, 724, 318

Neugebauer, G., Habing, H. J., van Duinen, R., et al. 1984, *ApJ*, 278, L1, aDS Bibcode: 1984ApJ...278L..1N

Obuchi, S., Ichikawa, K., Yamada, S., et al. 2025, Discovery of an X-ray Luminous Radio-Loud Quasar at $z=3.4$: A Possible Transitional Super-Eddington Phase, version Number: 1

O'Dea, C. 1998, *PASP*, 110, 493

Orienti, M., D'Ammando, F., Larsson, J., et al. 2015, *MNRAS*, 453, 4038

Osterbrock, D. E. & Ferland, G. J. 2006, Astrophysics of gaseous nebulae and active galactic nuclei, publication Title: Astrophysics of gaseous nebulae and active galactic nuclei aDS Bibcode: 2006agna.book.....O

Paliya, V. S., Stalin, C. S., Domínguez, A., & Saikia, D. J. 2023, *MNRAS*, 527, 7055

Panda, S., Marziani, P., & Czerny, B. 2019, *ApJ*, 882, 79

Peterson, B. M., Denney, K. D., De Rosa, G., et al. 2013, *ApJ*, 779, 109

Reynolds, C., Punsly, B., Miniutti, G., O'Dea, C. P., & Hurley-Walker, N. 2017, *ApJ*, 836, 155

Rigopoulou, D., Lawrence, A., White, G. J., Rowan-Robinson, M., & Church, S. E. 1996, *A&A*, 305, 747, aDS Bibcode: 1996A&A...305..747R

Runnoe, J. C., Brotherton, M. S., & Shang, Z. 2012, *MNRAS*, 422, 478

Rybicki, G. B. & Lightman, A. P. 1979, Radiative processes in astrophysics, publication Title: A Wiley-Interscience Publication aDS Bibcode: 1979rpaa.book.....R

Sani, E., Lutz, D., Risaliti, G., et al. 2010, *MNRAS*, 403, 1246, aDS Bibcode: 2010MNRAS.403.1246S

Sargsyan, L. A. & Weedman, D. W. 2009, *ApJ*, 701, 1398

Serjeant, S. & Hatziminaoglou, E. 2009, *MNRAS*, 397, 265

Shapovalova, A. I., Popović, L. v., Burenkov, A. N., et al. 2012, *ApJS*, 202, 10

Shen, Y. 2013, *BASI*, 41, 61, arXiv:1302.2643 [astro-ph]

Shen, Y., Grier, C. J., Horne, K., et al. 2024, *ApJS*, 272, 26

Shimwell, T. W., Hardcastle, M. J., Tasse, C., et al. 2022, *A&A*, 659, A1

Singha, M., Husemann, B., Urrutia, T., et al. 2022, *A&A*, 659, A123

Smith, J. D. T., Draine, B. T., Dale, D. A., et al. 2007, *ApJ*, 656, 770, aDS Bibcode: 2007ApJ...656..770S

Smoli, V., Delvecchio, I., Zamorani, G., et al. 2017, *A&A*, 602, A2

Stickel, M., Lemke, D., Klaas, U., et al. 2000, *A&A*, 359, 865, aDS Bibcode: 2000A&A...359..865S

Sulentic, J. W., Dultzin-Hacyan, D., Bongardo, C., et al. 2006, *RMxAA*, 42, 23, aDS Bibcode: 2006RMxAA..42..23S

Sulentic, J. W., Marziani, P., & Dultzin-Hacyan, D. 2000a, *ARA&A*, 38, 521

Sulentic, J. W., Marziani, P., Zamanov, R., et al. 2002, *ApJ*, 566, L71

Sulentic, J. W., Zwitter, T., Marziani, P., & Dultzin-Hacyan, D. 2000b, *ApJ*, 536, L5

Sun, J. & Shen, Y. 2015, *ApJ*, 804, L15

Temple, M. J., Ferland, G. J., Rankine, A. L., Chatzikos, M., & Hewett, P. C. 2021, *MNRAS*, 505, 3247

Temple, M. J., Ferland, G. J., Rankine, A. L., et al. 2020, *MNRAS*, 496, 2565

Van Hoof, P. A. M., Ferland, G. J., Williams, R. J. R., et al. 2015, *MNRAS*, 449, 2112

Van Hoof, P. A. M., Williams, R. J. R., Volk, K., et al. 2014, *MNRAS*, 444, 420

Veilleux, S., Meléndez, M., Tripp, T. M., Hamann, F., & Rupke, D. S. N. 2016, *ApJ*, 825, 42

Vestergaard, M. & Peterson, B. M. 2006, *ApJ*, 641, 689

Vieth, A., Järvelä, E., Berton, M., et al. 2022, *A&A*, 662, A20

Vieth, G., Piconcelli, E., Bischetti, M., et al. 2018, *A&A*, 617, A81

Wang, J.-G., Dong, X.-B., Wang, T.-G., et al. 2009, *ApJ*, 707, 1334, aDS Bibcode: 2009ApJ...707.1334W

Wang, J.-M., Qiu, J., Du, P., & Ho, L. C. 2014, *ApJ*, 797, 65

Wang, R., Carilli, C. L., Neri, R., et al. 2010, *ApJ*, 714, 699

Ward, S. R., Costa, T., Harrison, C. M., & Mainieri, V. 2024, AGN-driven outflows in clumpy media: multiphase structure and scaling relations, version Number: 2

Wills, B. J. & Browne, I. W. A. 1986, *ApJ*, 302, 56

Wolf, J., Nandra, K., Salvato, M., et al. 2023, *A&A*, 669, A127

Wolf, J., Nandra, K., Salvato, M., et al. 2021, *A&A*, 647, A5

Wright, E. L., Eisenhardt, P. R. M., Mainzer, A. K., et al. 2010, *AJ*, 140, 1868, aDS Bibcode: 2010AJ....140.1868W

Wu, Q. 2009, *MNRAS*, 398, 1905

Xie, Y. & Ho, L. C. 2022, *ApJ*, 925, 218, aDS Bibcode: 2022ApJ...925..218X

Yang, H., Yuan, F., Kwan, T., & Dai, L. 2023, *MNRAS*, 523, 208

Yue, B. H., Duncan, K. J., Best, P. N., et al. 2025, *MNRAS*, 537, 858

Yun, M. S., Reddy, N. A., & Condon, J. J. 2001, *ApJ*, 554, 803

Zamanov, R., Marziani, P., Sulentic, J. W., et al. 2002, *ApJ*, 576, L9

Zamfir, S., Sulentic, J. W., & Marziani, P. 2008, *MNRAS*, 387, 856

Zamfir, S., Sulentic, J. W., Marziani, P., & Dultzin, D. 2010, *MNRAS*, 403, 1759

Zhang, K., Dong, X.-B., Wang, T.-G., & Gaskell, C. M. 2011, *ApJ*, 737, 71

Appendix A: Radio images, VLA observations setup and variability

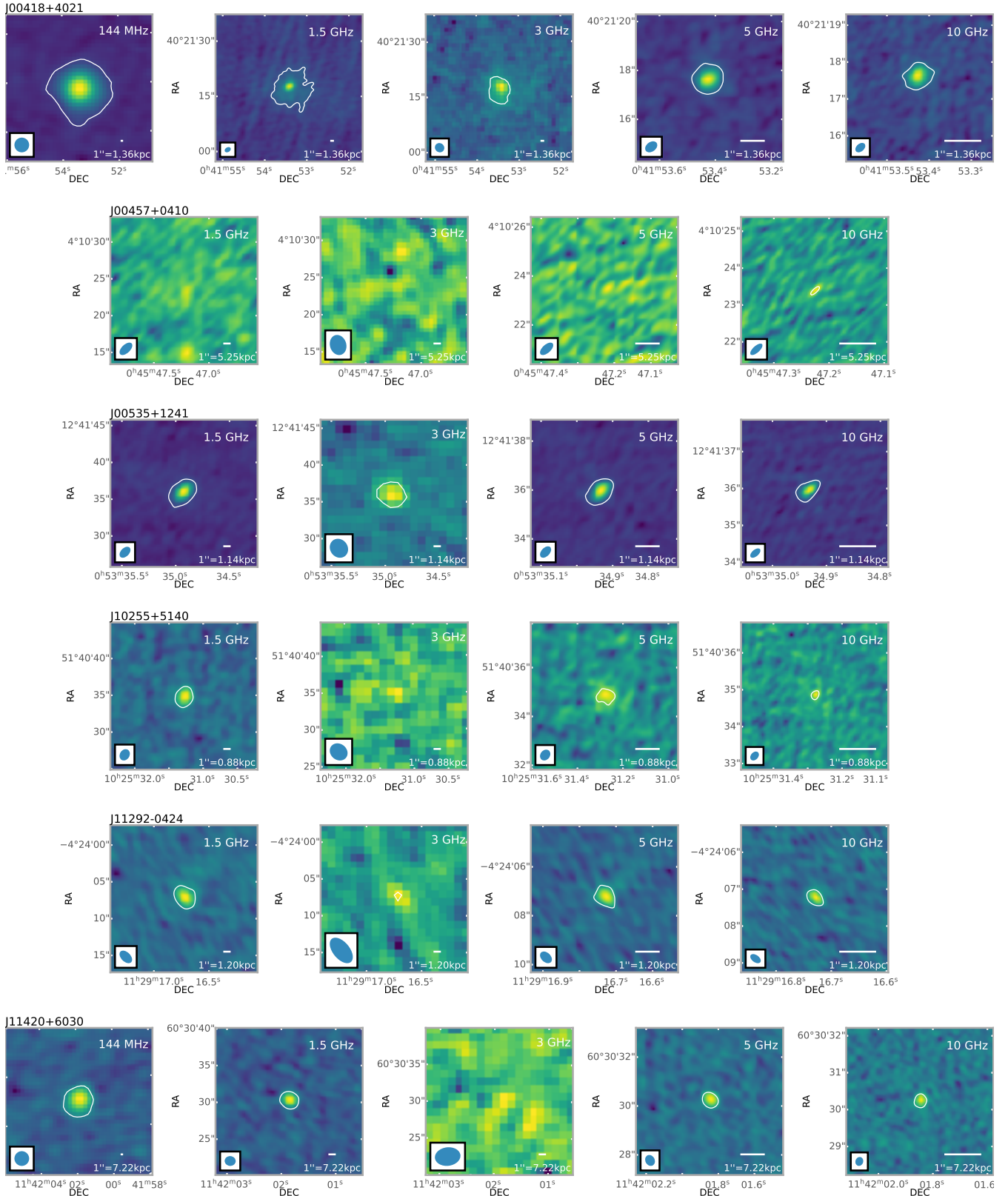


Fig. A.1: LOFAR (144 MHz) - when available - as well as our VLA L (1.5 GHz), C (5 GHz) and X (10 GHz) band images and VLASS (S-band, 3 GHz) of the 18 targets of the sample, each with a 5σ contour encompassing the main target in white. The sizes of the beams are shown in the bottom-left corner, while the scales are in the bottom-right corner. The cutouts have sizes of $1' \times 1'$, $20'' \times 20''$, $20'' \times 20''$, $6'' \times 6''$ and $4'' \times 4''$ at 144 MHz, 1.5 GHz, 3 GHz, 5 GHz and 10 GHz respectively - except for sources with larger detected diffuse emission (J00418+4021, J12562+5652), which cutouts have been increased to encompass it.

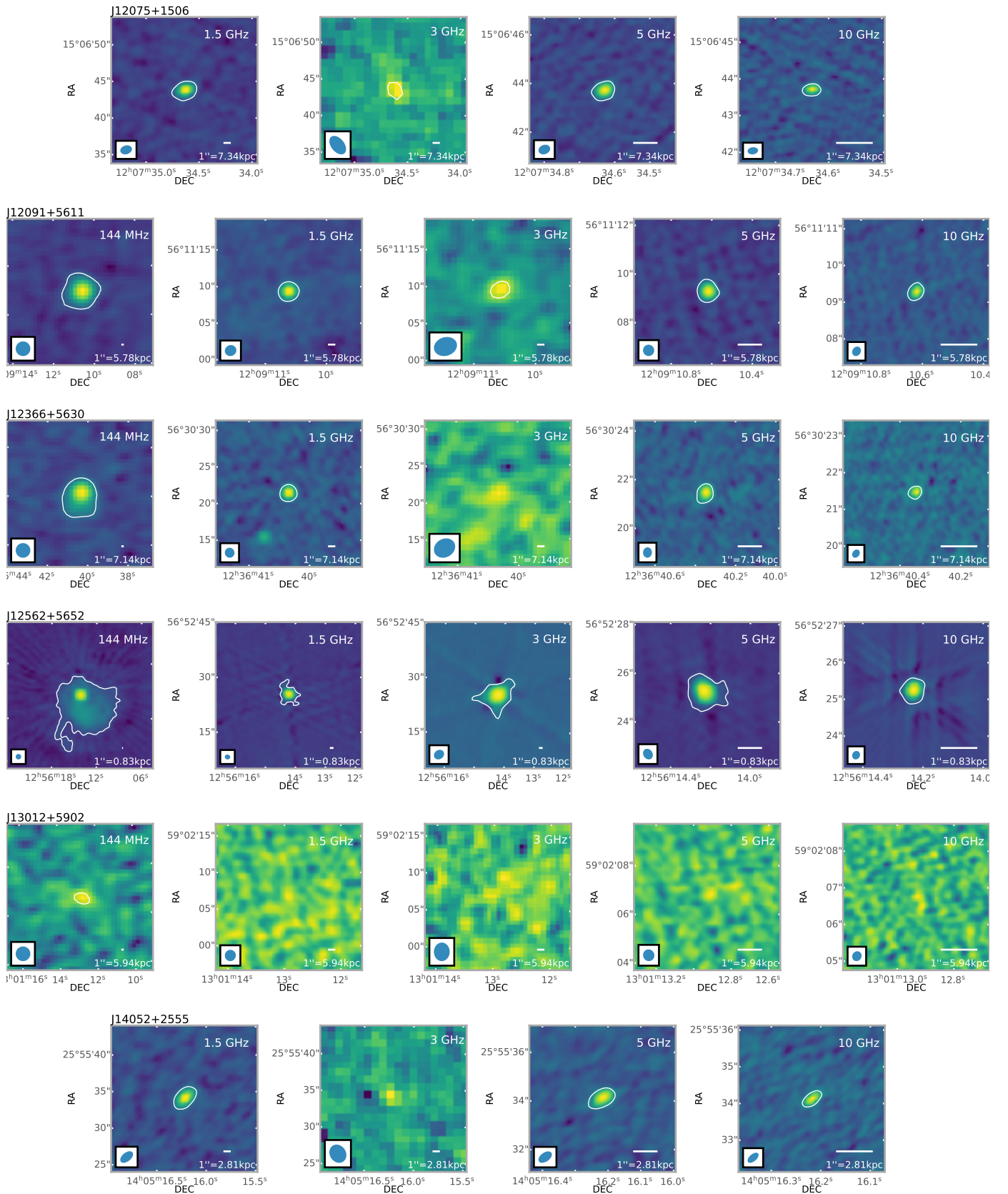


Fig. A.1: Continuation of Figure A.1.

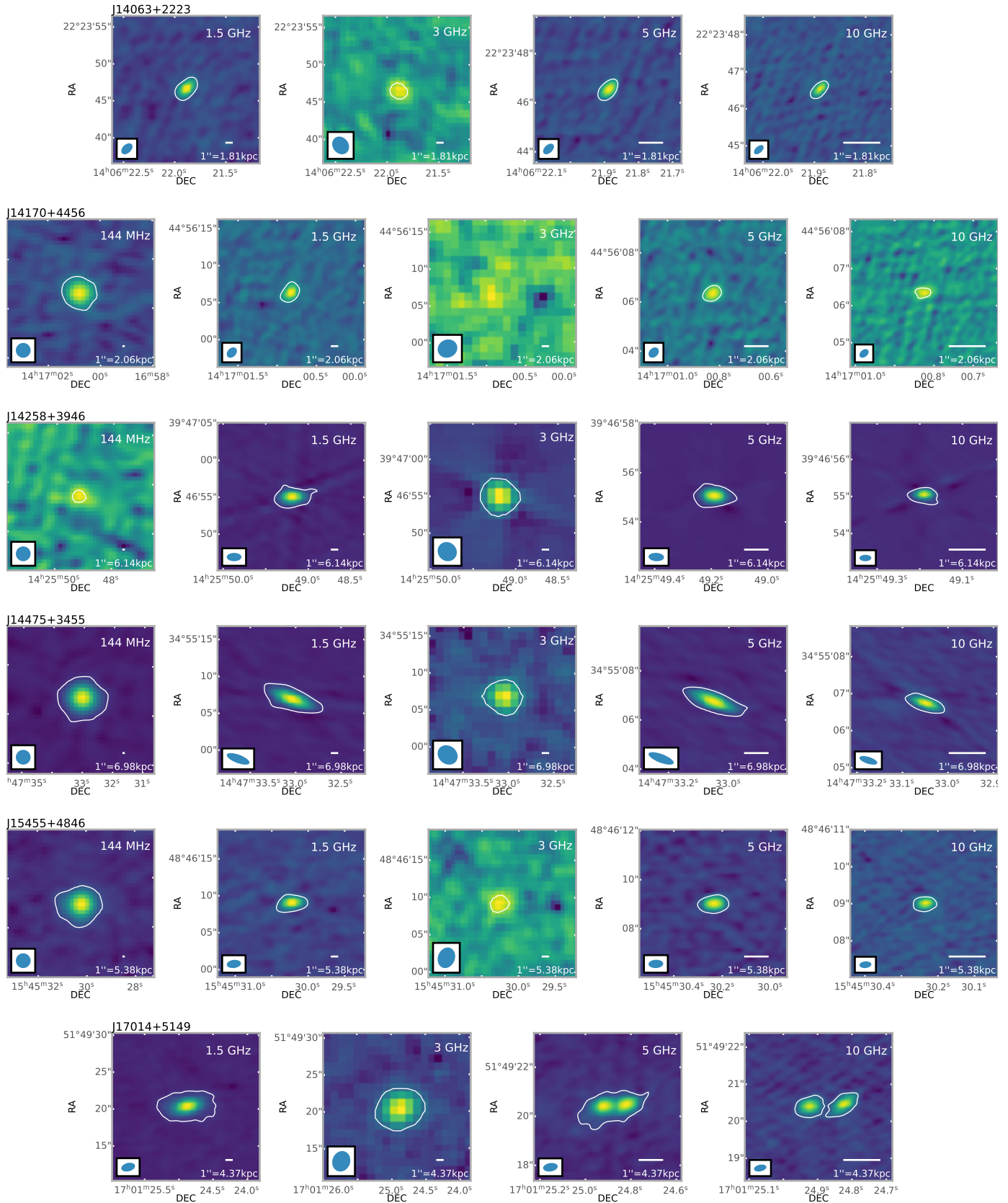


Fig. A.1: Continuation of Figure A.1.

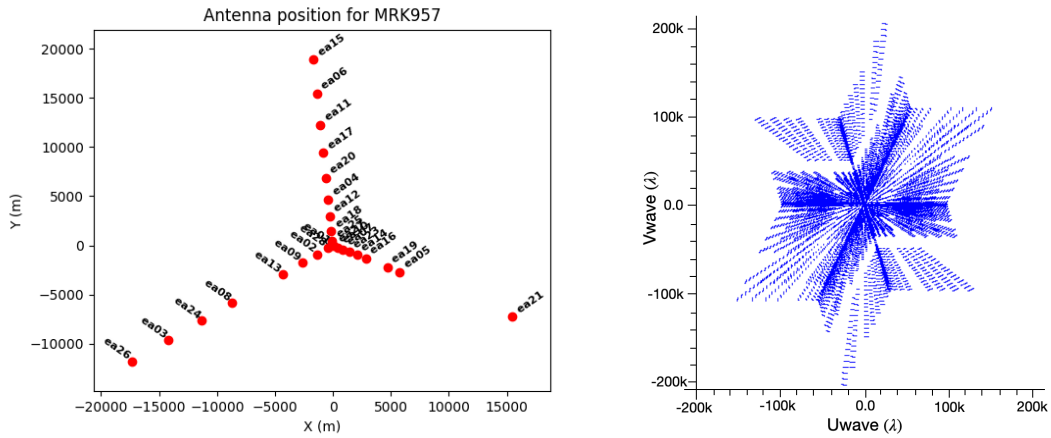


Fig. A.2: Antenna positions during the observations of J00418+4021 on 2020-12-04, and *uv* plane coverage of the L-band scan (with an averaging on 128 channels).

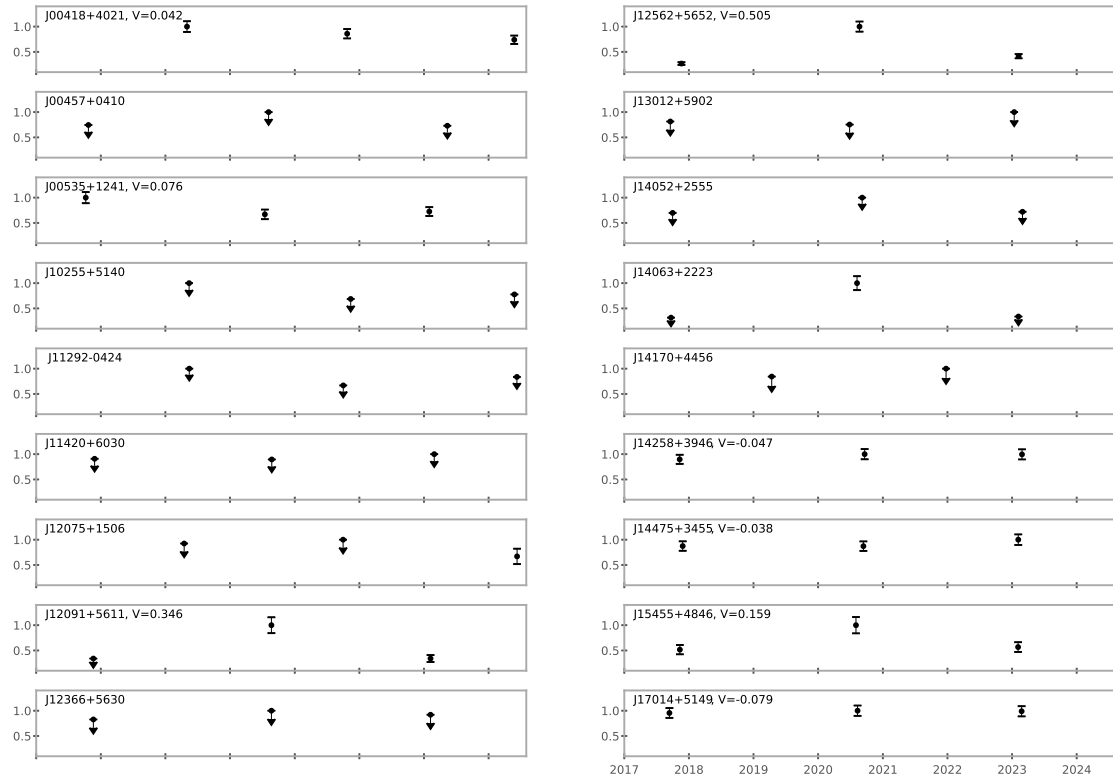


Fig. A.3: Sources variability across VLASS observations. Fluxes have been normalized by the maximum flux observed with VLASS, and the variability index V is shown for sources with detections in at least two epochs.

Appendix B: Radio images properties, measured radio flux densities and spectrum, spectral indices and radio luminosity, IR and FIR fluxes

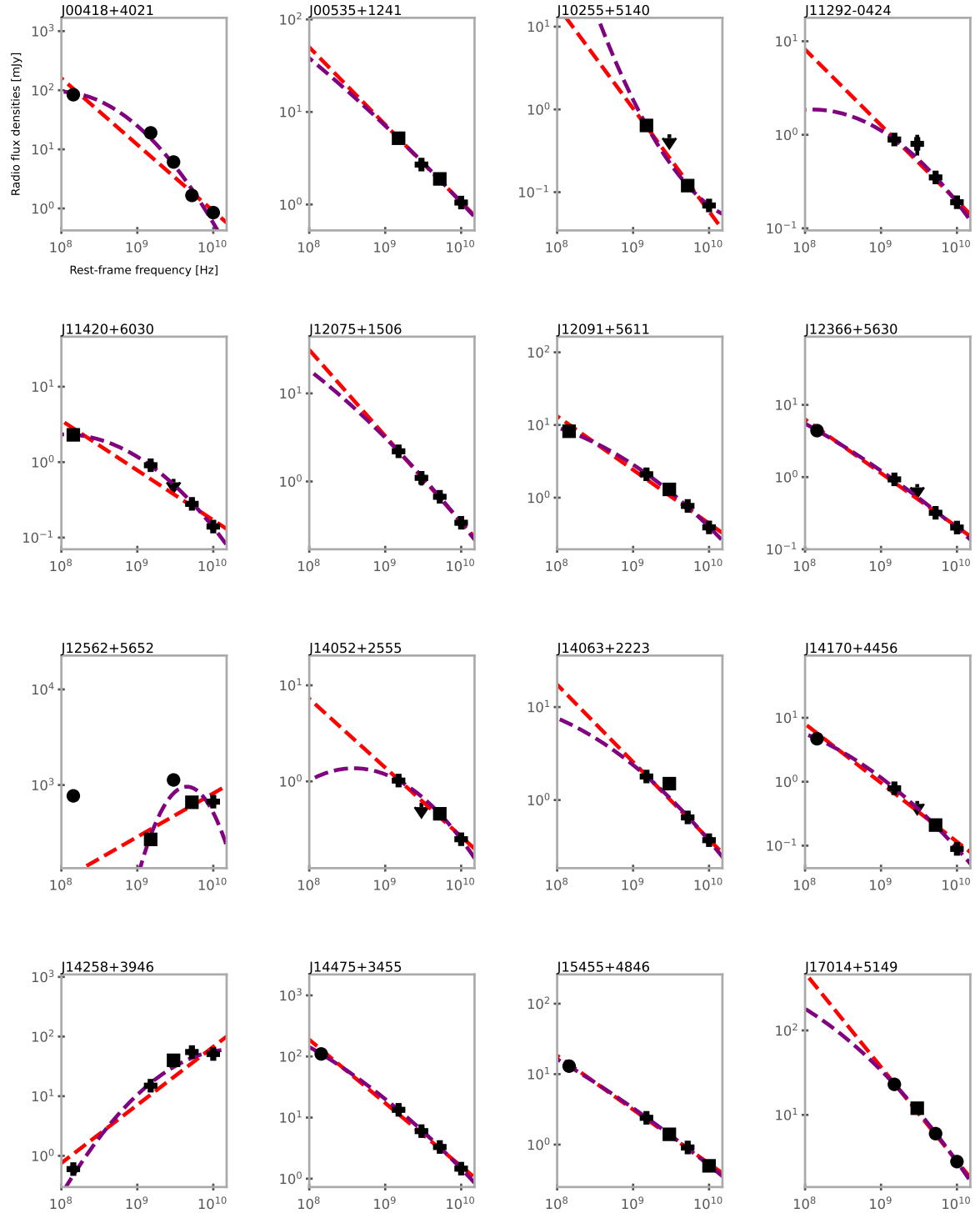


Fig. B.1: The radio spectra of the 16 sources detected in three bands or more. The dashed red line indicate the linear fit while the dashed purple line present the parabolic fit. Upper limits are shown but have been excluded during fitting procedure. The marker shape indicate the morphology of the source at the given frequency : circle for extended, square for intermediates and cross for compact sources.

Table B.1: Final radio images properties*

Object	LOFAR 144 MHz			VLA L-band 1.5 GHz			VLASS S-band 3 GHz			VLA C-band 5 GHz			VLA X-band 10 GHz			
	Beam	rms	DR	Beam	rms	DR	Epoch	Beam	rms	DR	Beam	rms	DR	Beam	rms	DR
J00418+4021	6x6	100	20000	2x1	50	10000	2.2 QL**	3x2	100	2000	0.5x0.4	20	100	0.3x0.2	7	60
J00457+0410	-	-	-	2x1	30	800	2.1 SE	3x2	100	300	0.7x0.3	10	100	0.4x0.2	7	20
J00535+1241	-	-	-	2x1	30	100	2.1 QL	3x2	200	200	0.6x0.3	10	200	0.3x0.2	7	100
J10255+5140	-	-	-	2x1	20	1000	2.2 QL	3x2	100	1000	0.5x0.4	10	100	0.3x0.2	7	20
J11292-0424	-	-	-	2x1	30	5000	2.2 QL	4x2	100	3000	0.6x0.4	10	300	0.3x0.2	9	100
J11420+6030	6x6	50	100000	1x1	20	2000	2.1 QL	3x3	100	300	0.5x0.4	10	30	0.2x0.2	7	20
J12075+1506	-	-	-	2x1	30	800	2.2 QL	3x2	100	800	0.5x0.4	10	60	0.3x0.2	8	40
J12091+5611	6x6	60	70000	2x1	50	600	2.1 SE	3x3	200	700	0.5x0.5	10	100	0.3x0.2	8	50
J12366+5630	6x6	40	50000	1x1	30	500	2.1 SE	3x2	200	200	0.4x0.4	8	2000	0.2x0.2	8	2000
J12562+5652	6x6	200	60000	1x1	70	4000	2.1 SE	3x2	300	4000	0.5x0.4	200	4000	0.2x0.2	500	1000
J13012+5902	6x6	50	30000	2x2	30	200	2.1 SE	3x2	90	300	0.5x0.5	10	20	0.3x0.2	7	20
J14052+2555	-	-	-	2x1	20	600	2.1 QL	3x2	100	600	0.6x0.4	10	40	0.4x0.2	9	30
J14063+2223	-	-	-	2x1	30	4000	2.1 SE	3x2	100	400	0.5x0.3	10	60	0.3x0.2	7	60
J14170+4456	6x6	70	20000	2x1	20	200	2.2 QL	3x2	90	1000	0.5x0.4	10	200	0.3x0.2	8	60
J14258+3946	6x6	90	10000	2x1	50	300	2.1 QL	3x2	600	200	0.6x0.3	80	700	0.3x0.2	100	400
J14475+3455	6x6	200	20000	3x1	30	400	2.1 QL	3x2	100	200	1x0.3	10	300	0.5x0.2	10	100
J15455+4846	6x6	60	80000	2x1	30	5000	2.1 SE	3x2	100	800	0.6x0.3	9	100	0.3x0.2	7	60
J17014+5149	-	-	-	2x1	30	1000	2.1 QL	3x2	100	600	0.6x0.3	10	200	0.3x0.2	10	90

Notes. * Beams are given in arcseconds, while the rms of the images are given in $\mu\text{Jy}/\text{beam}$. ** For VLASS images, QL stands for a Quick Look image data product, while SE stands for a Single Epoch continuum image data product.

Table B.2: Measured radio flux densities of the sources in mJy from the original images at their respective resolutions based on 5σ contours, their respective morphology type* and the calculated Kellermanns parameter R_k .

Object	LOFAR 144 MHz		VLA L-band 1.5 GHz		VLASS S-band 3 GHz		VLA C-band 5 GHz		VLA X-band 10 GHz		R_k
	Flux	Type	Flux	Type	Flux	Type	Flux	Type	Flux	Type	
J00418+4021	84 ± 8	E	19 ± 1	E	$6.1 \pm 0.7^{\text{QL}}**$	E	1.66 ± 0.09	E	0.85 ± 0.05	E	1.83
J00457+0410	-	-	< 0.1	-	$< 0.7^{\text{SE}}$	-	< 0.05	-	0.050 ± 0.008	C	$\lesssim -0.50$
J00535+1241	-	-	5.2 ± 0.3	I	$2.7 \pm 0.3^{\text{QL}}$	C	1.89 ± 0.10	I	1.05 ± 0.05	C	0.07
J10255+5140	-	-	0.64 ± 0.05	I	$< 0.5^{\text{QL}}$	-	0.12 ± 0.01	I	0.069 ± 0.008	C	-0.24
J11292-0424	-	-	0.89 ± 0.05	C	$0.8 \pm 0.2^{\text{QL}}$	C	0.35 ± 0.02	C	0.19 ± 0.01	C	-0.11
J11420+6030	2.3 ± 0.2	I	0.91 ± 0.05	C	$< 0.6^{\text{QL}}$	-	0.28 ± 0.02	C	0.14 ± 0.01	C	1.15
J12075+1506	-	-	2.2 ± 0.1	C	$1.1 \pm 0.2^{\text{QL}}$	C	0.67 ± 0.04	C	0.34 ± 0.02	C	0.81
J12091+5611	8.2 ± 0.8	I	2.1 ± 0.1	C	$1.3 \pm 0.2^{\text{SE}}$	I	0.77 ± 0.04	C	0.39 ± 0.02	C	1.71
J12366+5630	4.4 ± 0.4	E	0.93 ± 0.05	C	$< 0.8^{\text{SE}}$	-	0.32 ± 0.02	C	0.20 ± 0.01	C	1.52
J12562+5652	770 ± 80	E	270 ± 10	I	$1130 \pm 30^{\text{SE}}$	E	660 ± 30	I	670 ± 30	C	1.53
J13012+5902	0.38 ± 0.06	C	< 0.1	-	$< 0.5^{\text{SE}}$	-	< 0.05	-	< 0.04	-	$\lesssim -1.88$
J14052+2555	-	-	1.02 ± 0.06	C	$< 0.6^{\text{QL}}$	-	0.46 ± 0.03	I	0.25 ± 0.02	C	-1.14
J14063+2223	-	-	1.79 ± 0.09	C	$1.5 \pm 0.2^{\text{SE}}$	I	0.65 ± 0.03	C	0.37 ± 0.02	C	-0.34
J14170+4456	4.7 ± 0.5	E	0.79 ± 0.04	C	$< 0.5^{\text{QL}}$	-	0.21 ± 0.02	I	0.089 ± 0.010	C	-0.94
J14258+3946	0.6 ± 0.1	C	15.0 ± 0.8	C	$40 \pm 4^{\text{QL}}$	I	55 ± 3	C	51 ± 3	C	2.99
J14475+3455	110 ± 10	E	13.4 ± 0.7	C	$6.0 \pm 0.6^{\text{QL}}$	C	3.3 ± 0.2	C	1.46 ± 0.07	C	1.34
J15455+4846	13 ± 1	E	2.4 ± 0.1	C	$1.4 \pm 0.2^{\text{SE}}$	I	0.91 ± 0.05	C	0.50 ± 0.03	I	1.08
J17014+5149	-	-	23 ± 1	E	$12 \pm 1^{\text{QL}}$	I	6.0 ± 0.3	E	2.8 ± 0.1	E	1.24

Notes. * C indicates compact, I is intermediate morphology, and E indicates the presence of diffuse emission. ** For VLASS images, QL stands for a Quick Look image data product, while SE stands for a Single Epoch continuum image data product. The parameter R_k has been computed as the ratio between the K-corrected flux at 1.4GHz and the optical one at 5100 Å.

Table B.3: IR and FIR fluxes used during the analysis.

Object	$S_{60\mu m}$ [mJy]	$L_{60\mu m}$ [erg s $^{-1}$]	$S_{100\mu m}$ [mJy]	$L_{100\mu m}$ [erg s $^{-1}$]	$L(\text{FIR})$ [erg s $^{-1}$]	M_{W4}	S_{22} [mJy]
J00418+4021	2100 ± 170	$1.16 \pm 0.09 \text{ E+45}$	3200 ± 1000	$1.8 \pm 0.5 \text{ E+45}$	$5 \pm 2 \text{ E+45}$	3.96 ± 0.02	219 ± 4
J00457+0410	< 200	$< 3 \text{ E+45}$	< 300	$< 6 \text{ E+45}$	$< 4 \text{ E+45}$	6.19 ± 0.09	28 ± 2
J00535+1241	2160 ± 50	$8.2 \pm 0.2 \text{ E+44}$	2960 ± 50	$1.12 \pm 0.2 \text{ E+44}$	$3.9 \pm 0.2 \text{ E+45}$	2.37 ± 0.02	940 ± 20
J10255+5140	150 ± 40	$3.4 \pm 0.9 \text{ E+43}$	200 ± 100	$4 \pm 2 \text{ E+43}$	$2 \pm 2 \text{ E+44}$	5.57 ± 0.03	50 ± 2
J11292-0424	670 ± 30	$2.8 \pm 0.1 \text{ E+44}$	1200 ± 100	$4.9 \pm 0.6 \text{ E+44}$	$1.4 \pm 0.2 \text{ E+45}$	3.71 ± 0.02	275 ± 6
J11420+6030	-	-	-	-	-	7.7 ± 0.2	7 ± 1
J12075+1506	-	-	-	-	-	6.46 ± 0.06	22 ± 1
J12091+5611	-	-	-	-	-	9.2 ± 0.5	1.8 ± 0.9
J12366+5630	-	-	-	-	-	8.5 ± 0.2	3.5 ± 0.7
J12562+5652	32000 ± 2000	$6.2 \pm 0.3 \text{ E+45}$	30000 ± 1000	$5.9 \pm 0.2 \text{ E+45}$	$3.5 \pm 0.5 \text{ E+46}$	0.27 ± 0.01	6530 ± 70
J13012+5902	30 ± 50	$1 \pm 2 \text{ E+45}$	-	-	$8 \pm 200 \text{ E+44}$	6.40 ± 0.05	23 ± 1
J14052+2555	230 ± 50	$7 \pm 2 \text{ E+44}$	-	-	$1 \pm 4 \text{ E+45}$	4.65 ± 0.03	115 ± 3
J14063+2223	< 100	$< 1.5 \text{ E+44}$	< 100	$< 1.3 \text{ E+44}$	$< 4.0 \text{ E+44}$	6.04 ± 0.05	32 ± 1
J14170+4456	110 ± 30	$1.6 \pm 0.5 \text{ E+44}$	150 ± 70	$2 \pm 1 \text{ E+44}$	$4 \pm 4 \text{ E+44}$	5.28 ± 0.03	65 ± 2
J14258+3946	-	-	-	-	-	8.4 ± 0.3	3.6 ± 0.9
J14475+3455	< 200	$< 1.5 \text{ E+46}$	< 600	$< 4.1 \text{ E+46}$	$< 1.4 \text{ E+46}$	5.37 ± 0.03	59 ± 1
J15455+4846	350 ± 30	$7.0 \pm 0.5 \text{ E+45}$	370 ± 80	$7.0 \pm 2 \text{ E+45}$	$7 \pm 2 \text{ E+45}$	4.72 ± 0.02	109 ± 3
J17014+5149	480 ± 40	$4.8 \pm 0.4 \text{ E+45}$	400 ± 100	$4 \pm 1 \text{ E+45}$	$6 \pm 2 \text{ E+45}$	4.09 ± 0.02	193 ± 3

Notes. Column 1: Object coordinate name. Column 2: $60\mu m$ flux densities from IRAS or ISO data. Column 3: $60\mu m$ luminosity derived from equation 7. Column 4: $100\mu m$ flux densities from IRAS or ISO data. Column 5: $100\mu m$ luminosity derived from equation 7. Column 6: $L(\text{FIR})$ defined from a linear combination of the $60\mu m$ and $100\mu m$ fluxes according to Helou et al. 1985. Column 7: WISE band 4 ($22\mu m$) magnitude. Column 8: $22\mu m$ flux densities derived from Column 7 magnitudes, using $F_{\nu_0} \times 10^{-M_{W4}/2.5}$, where $F_{\nu_0} = 8.363 \text{ Jy}$ (Jarrett et al. 2011) is the zero magnitude flux density in band 4 corresponding to the constant that gives the same response as that of Vega.

Table B.4: Measured spectral indices and radio luminosity of the sources

Object	$\alpha_{0.144-1.5}$	$\alpha_{1.5-3}$	α_{3-5}	α_{5-10}	α	$L_{1.4\text{GHz}}$ [W Hz $^{-1}$]	$p\text{SFR}_{\text{radio}}$ $M_{\odot}\text{yr}^{-1}$
J00418+4021	-0.63 ± 0.05	-1.6 ± 0.2	-2.3 ± 0.2	-1.0 ± 0.1	-1.1 ± 0.2	1.02E+23	2.72E+01
J00457+0410	-	-	-	> 0.0	-	-	-
J00535+1241	-	-0.9 ± 0.2	-0.6 ± 0.2	-0.9 ± 0.1	-0.84 ± 0.03	4.55E+22	1.40E+01
J10255+5140	-	< -0.4	> -3	-0.9 ± 0.2	-1.2 ± 0.1	3.18E+21	1.57E+00
J11292-0424	-	-0.2 ± 0.4	-1.5 ± 0.5	-0.9 ± 0.1	-0.81 ± 0.05	8.88E+21	3.66E+00
J11420+6030	-0.40 ± 0.04	< -0.6	> -1	-1.1 ± 0.2	-0.7 ± 0.1	1.50E+24	2.49E+02
J12075+1506	-	-1.0 ± 0.3	-0.9 ± 0.3	-1.0 ± 0.1	-0.98 ± 0.02	6.24E+24	8.06E+02
J12091+5611	-0.58 ± 0.05	-0.7 ± 0.2	-0.9 ± 0.3	-1.1 ± 0.1	-0.74 ± 0.06	1.46E+24	2.43E+02
J12366+5630	-0.66 ± 0.05	< -0.2	> -2	-0.7 ± 0.1	-0.74 ± 0.03	1.65E+24	2.69E+02
J12562+5652	-0.45 ± 0.05	2.06 ± 0.07	-0.97 ± 0.09	0.02 ± 0.10	0.5 ± 0.3	1.33E+24	2.26E+02
J13012+5902	< -0.6	-	-	-	-	-	-
J14052+2555	-	< -0.8	> -0.5	-0.9 ± 0.2	-0.72 ± 0.07	8.01E+22	2.24E+01
J14063+2223	-	-0.3 ± 0.2	-1.5 ± 0.3	-0.9 ± 0.1	-0.83 ± 0.06	4.64E+22	1.43E+01
J14170+4456	-0.76 ± 0.05	< -0.7	> -2	-1.3 ± 0.2	-0.92 ± 0.09	2.43E+22	8.38E+00
J14258+3946	1.37 ± 0.07	1.4 ± 0.2	0.6 ± 0.2	-0.1 ± 0.1	1.0 ± 0.2	6.80E+24	8.66E+02
J14475+3455	-0.90 ± 0.04	-1.2 ± 0.2	-1.1 ± 0.2	-1.3 ± 0.1	-1.04 ± 0.05	2.64E+25	2.64E+03
J15455+4846	-0.72 ± 0.04	-0.8 ± 0.2	-0.8 ± 0.3	-0.9 ± 0.1	-0.77 ± 0.02	1.35E+24	2.28E+02
J17014+5149	-	-0.9 ± 0.1	-1.2 ± 0.2	-1.18 ± 0.09	-1.11 ± 0.03	7.19E+24	9.06E+02

Notes. Column 1: Object coordinate name. Column 2: spectral slope at 0.1441.5 GHz. Column 3: spectral slope at 1.53 GHz. Column 4: spectral slope at 35 GHz. Column 5: spectral slope at 510 GHz. Column 6: spectral slope fit over the whole frequency range available for sources with detection in at least three bands. Column 7: Calculated radio luminosity in W Hz $^{-1}$ at 1.4 GHz using equation 3. Column 8: Pseudo radio SFR in $M_{\odot}\text{yr}^{-1}$.

Appendix C: Optical spectroscopy

Fig. C.1 shows the results of a multicomponent nonlinear analysis of the $H\beta$ spectral range, after continuum subtraction. Several previous papers have successfully applied the same technique (Negrete et al. 2018); here we recall only the salient points. The main components of the model are a power law continuum, FeII emission according to a standard template (Boroson & Green 1992), $H\beta$ emission well-fit by a Lorentzian profile (see e.g., Sulentic et al. 2002; Shapovalova et al. 2012; Wang et al. 2014; Cracco et al. 2016; Negrete et al. 2018; Crepaldi et al. 2025, for a variety of approaches), and $[OIII]\lambda\lambda4959,5007$ emission. In sources where FeII is much weaker, the Lorentzian is found at a wavelength consistent with the one of the quasar rest frame; small shifts ($\lesssim \pm 100$) are possible due to uncertainties in the systemic redshift ($\lesssim 50 \text{ km s}^{-1}$), compounded with a slight mismatch originating in the fitting process. The outflow emission originating from the broad-line region (BLR) is modeled as a blueshifted skew Gaussian, on the basis of the trapezoidal profile most often observed in the $\text{CIV}\lambda1549$ profile of xA sources (e.g., Zamanov et al. 2002; Leighly & Moore 2004; Martínez-Aldama et al. 2018). The narrow-line region (NLR) emission is similarly modeled by separating a symmetric Gaussian and a skew Gaussian (Azzalini 1985), usually shifted toward shorter wavelengths, and helpful to model the outflow component that is prominent in the $[OIII]\lambda5007$ emission (Zhang et al. 2011). The shaded areas in Fig. C.1 emphasize the $H\beta$ outflow profile (magenta) and the full blueshifted profile of $[OIII]\lambda\lambda4959,5007$ (cyan). The $H\beta$ BLUE (shaded magenta) is barely detectable in several sources, but produce are remarkable blueward asymmetry especially in the sources with strong FeII emission. The $[OIII]\lambda\lambda4959,5007$ full profile (shaded cyan) is often dominated by the SBC shifted to the blue. The $[OIII]\lambda5007$ FWHM is large, and its equivalent width is low, to the point that the line is, in several cases, barely detectable over the strong FeII emission. This result is in agreement with the basic tenet of the Eigenvector 1 paradigm (the anticorrelation between the peak intensity of $[OIII]\lambda5007$ and R_{FeII} , Boroson & Green 1992).

Table C.1 reports measurements carried out on full profile of the $H\beta$ line, as well as on the blueshifted component associated with the BLR outflows. The centroids, the asymmetry (AI) and kurthosis (KI) indexes reported in the Tables are computed according to the definition of Zamfir et al. (2010). The column providing information on the strength of FeII emission reports the intensity ratio $R_{\text{FeII}} = \text{FeII}\lambda4570/H\beta$, where $\text{FeII}\lambda4570$ is the intensity of the blend on the blue side of $H\beta$ (Fig. C.1), that is the parameter used for the selection of xA sources. The following columns report relative intensity normalized to the full broad profile of the $H\beta$ broad component (BC), symmetric and unshifted, and its FWHM. For the blueshifted broad component (BLUE), the relative contribution is listed along with FWHM, peak shift and skew parameter that describes the asymmetry of the skew normal function used to model its profile.

Table C.2 reports measurements carried out on the $[OIII]\lambda5007$ line, following a scheme analogous to Table C.1 for $H\beta$. The centroids, AI and KI are reported for the full $[OIII]\lambda5007$ profile following the spectrophotometric parameters. We distinguish a narrow component (NC) and a semi-broad component (SBC), with blueshifts ranging from almost 0 to a few thousands km s^{-1} . We report relative intensity for the NC and SBC, along with FWHM and Shift. For the $[OIII]\lambda5007$ SBC, the shift (defined as the mode of the skew normal distribution) is not representative of the bulk displacement of the line with respect to

the rest frame. In this case, we provide also the centroid at half maximum $c(\frac{1}{2})$.

Appendix C.1: Estimation of wind parameters

Appendix C.1.1: $[OIII]\lambda\lambda4959,5007$

The large blueshifts and blue-ward skewness of the $[OIII]\lambda\lambda4959,5007$ lines suggests the presence of an outflow for the emitting gas, possibly originating from nuclear winds, or from radiative feedback on the gas of the host galaxy bulge, where the receding side of the flow is obscured or absorbed (Zamanov et al. 2002; Cresci et al. 2015; Singha et al. 2022; Kakkad et al. 2022). The relations for line emitting gas mass, mass flow, thrust and kinetic power based on the BLUE component of $[OIII]\lambda5007$ are the ones provided by Marziani et al. (2017), scaled to $n_{\text{H}} = 10^4 \text{ cm}^{-3}$ (Sect. 3.6). They are standard relations (Cano-Díaz et al. 2012; Fiore et al. 2017), obtained assuming optically-thin emission confined in a bipolar outflow within a solid angle $2\cdot\Omega$.

The immediate inference from the $[OIII]\lambda5007$ outflow parameters (Tab. C.3) computed from the data listed in Table C.2 is that they show an especially strong dependence on luminosity, with the kinetic power reaching tenth of percent of the bolometric luminosity ($\sim 0.1 - 0.2\%$) in the case of the most luminous sources. This result is consistent with previous works (Carniani et al. 2015; Fiore et al. 2017; Bischetti et al. 2017; Vietri et al. 2018; Kakkad et al. 2020). The mass outflow rate is always $\dot{M} \lesssim 10 \text{ M}_{\odot} \text{ yr}^{-1}$, with only a few luminous sources reaching $\dot{M} \sim 5 \text{ M}_{\odot} \text{ yr}^{-1}$. The low values of the wind parameters are also a consequence of the low equivalent width of the $[OIII]\lambda5007$ emission (Boroson & Green 1992; Zamanov et al. 2002). Apparently, even if the sources of the present sample are close to maximum radiative output per unit black hole mass, they are capable of inducing modest mechanical effects, especially at low-luminosity.

Appendix C.1.2: $H\beta$

An estimation of the wind parameters for $H\beta$ BLUE is less standard, as the mildly-ionized wind emission has been usually traced by the resonance high-ionization line of $\text{CIV}\lambda1549$ (e.g., Marziani et al. 2016a; Vietri et al. 2018). The blueshifted $H\beta$ emission is presumably associated with the BLR: spatial scales are smaller, and the electron densities are expected to be much higher with respect to the $[OIII]\lambda5007$ emitting regions, but are less well-known. It is customary to assume a standard value for the BLR electron density $n \sim 10^9 > 10^8 \text{ cm}^{-3}$ (Netzer 2013), even if the density of the low-ionization part of the BLR is much higher (Marziani et al. 2010; Negrete et al. 2012; Temple et al. 2020, 2021), $\sim 10^{12} - 10^{13} \text{ cm}^{-3}$, and the outflow might be clumpy (e.g., Ward et al. 2024). The $H\beta$ emissivity can be written as $j_{H\beta} = n^2 \alpha_{H\beta}(T) h v_{H\beta}$ where n is the Hydrogen density ($n_e \sim n_{\text{H}} \sim n$) and $\alpha_{H\beta}(T)$ is the effective recombination coefficient for $H\beta$. At $T_e = 20,000 \text{ K}$, $\alpha_{H\beta} \approx 3.0 \times 10^{-14} \text{ cm}^3 \text{ s}^{-1}$ (Osterbrock & Ferland 2006), yielding an $H\beta$ emissivity $j_{H\beta} \sim 1.23 \cdot 10^{-7} n_9^2 \text{ erg s}^{-1} \text{ cm}^{-3}$. Therefore, the total mass of the line emitting gas is

$$M_{\text{HII}} \sim n \mu m_p \frac{L(H\beta) \text{ BLUE}}{j_{H\beta}} \sim 10^3 \frac{L_{44}(H\beta) \text{ BLUE}}{n_9} \text{ M}_{\odot}$$

where we assume $n_{\text{H}} = 10^9 \text{ cm}^{-3}$, the molecular weight $\mu = 1.4$, and m_p is the proton mass.

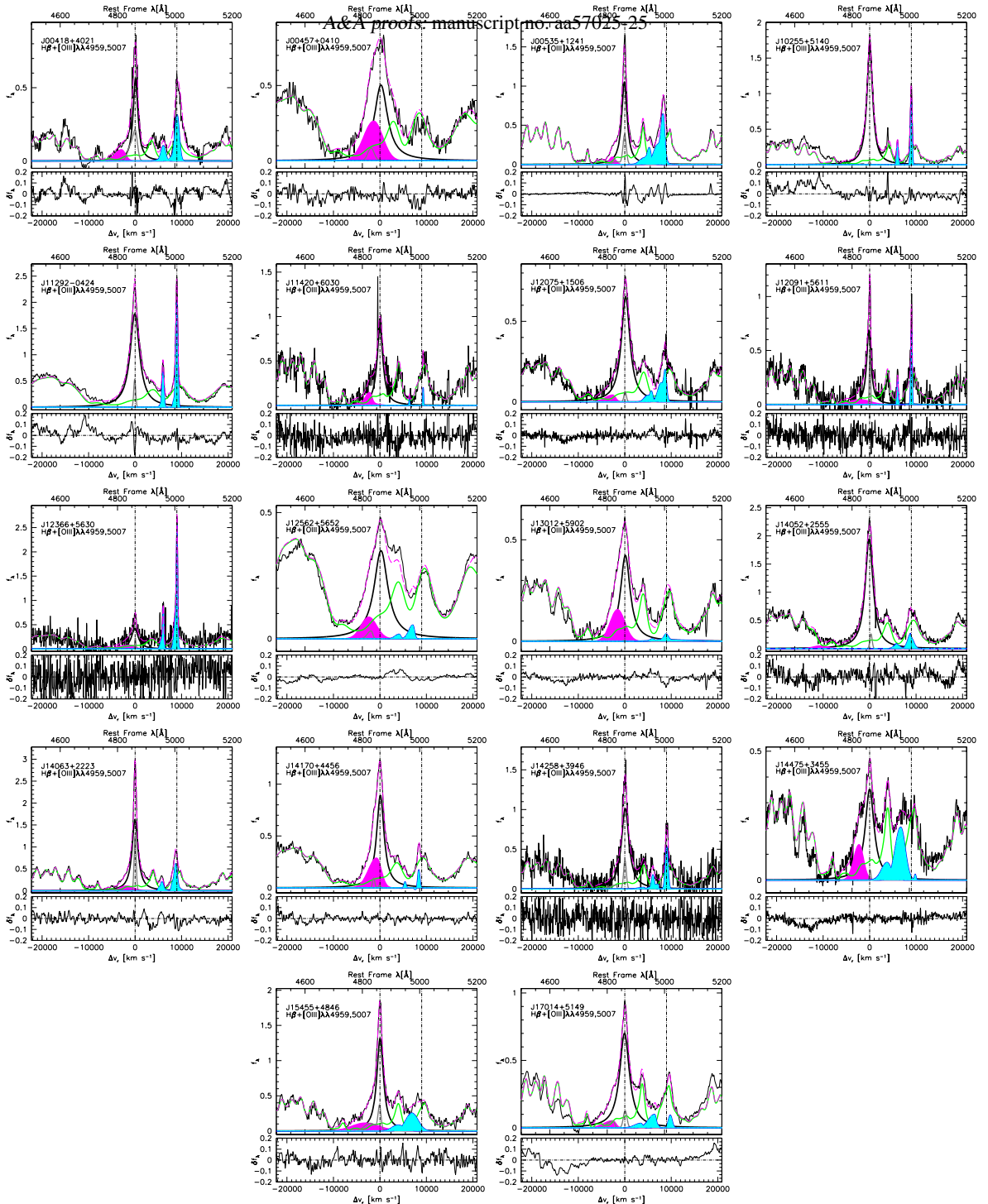


Fig. C.1: Continuum-subtracted, optical spectra of the 18 targets in the H β spectral range (upper panels). Abscissa is rest-frame wavelength (top scale) and radial velocity with respect to rest frame (bottom); ordinate is normalized specific flux, also in the rest frame. Thin black line: observed spectrum, thick black: broad component of H β ; thick blue shaded cyan: full profile of [OIII] $\lambda\lambda 4959,5007$; magenta: H β broad blueshifted emission; grey: H β narrow component; pale green: FeII template. The dashed magenta line traces the full empirical model of the spectrum. Lower panels: observed spectrum minus empirical model.

Using the same approach applied to [OIII] $\lambda 5007$, we can compute the outflows dynamical parameters as traced by the H β line. In this scenario, the gas emitting H β is presumably still being accelerated by radiation pressure, thereby gaining momentum. An additional factor must be incorporated into these calculations, either by adopting a simplified model for an unbound

gas subject to gravity and radiation pressure (Netzer & Marziani 2010; Marziani et al. 2017) or by applying an empirical recipe developed for the CIV $\lambda 1549$ line (Deconto-Machado et al. 2024), assuming a final outflow velocity of $c(\frac{1}{2})+2\sigma$ for the blueshifted component. We apply the simplest assumption including a factor $\kappa = 5$ (Marziani et al. 2017). The resulting relations for line

emitting mass, mass flow, thrust and kinetic power based on the BLUE component of H β are:

$$\begin{aligned}\dot{M} &\sim 60L_{\text{H}\beta,44}v_{1000}r_{0.1\text{pc}}^{-1}M_{\odot}\text{ yr}^{-1} \\ \dot{M}v &\sim 2 \cdot 10^{36}k_5L_{\text{H}\beta,44}v_{1000}^2r_{0.1\text{pc}}^{-1}\text{ g cm s}^{-2} \\ \dot{\epsilon} &\sim 5 \cdot 10^{44}k_5^2L_{\text{H}\beta,44}v_{1000}^2r_{0.1\text{pc}}^{-1}\text{ erg s}^{-1},\end{aligned}$$

assuming $n_{\text{H}} = 10^9 \text{ cm}^{-3}$, and velocity scaled to 1000 km s $^{-1}$.

The results obtained for the BLR outflow traced by the blueshifted excess of the H β line, reported in Table C.3, are consistent with the ones for the [OIII] $\lambda 5007$ outflow. In the H β case, there is however no straightforward comparison with earlier results based on the same line: the BLUE component is faint and difficult to measure, especially in cases with strong FeII. Since H β BLUE should be emitted in the same mildly-ionized outflow producing CIV $\lambda 1549$ and other UV high-ionization lines, a comparison can be made with the outflow parameters derived from CIV $\lambda 1549$ (Marziani et al. 2016b; Vietri et al. 2018; Deconto-Machado et al. 2023, 2024). The mass outflow rate is $\dot{M} \sim 1 \lesssim \text{a few } M_{\odot} \text{ yr}^{-1}$, with only J13012+5902 reaching $\dot{M} \sim 40 M_{\odot} \text{ yr}^{-1}$. Even if these values could be considered more as lower limit as anything else, the basic outcome is again consistent with previous results, where only at the largest luminosities the kinetic power might become as large as to imply a significant feedback effect on the host galaxy (Di Matteo et al. 2005; Ishibashi & Fabian 2012; King & Pounds 2015; Harrison et al. 2014; King & Muldrew 2016; Laha et al. 2020). The implication is that, while these sources are mostly candidate super-Eddington quasars, their BLR winds do not necessarily produce the strongest feedback, as the feedback effect primarily depends on luminosity – and thus on black hole mass – if $L/L_{\text{Edd}} \gtrsim 0.2$ (Marziani et al. 2025): L/L_{Edd} is constrained to be $L/L_{\text{Edd}} \lesssim 1$ (Mineshige et al. 2000), and hence to vary within a small range. On the converse M_{BH} and AGN luminosity (to which line luminosity is roughly proportional) can be factors ~ 100 higher in the most luminous quasars at the cosmic noon. Only in those cases the mechanical power of the NLR and BLR winds may reach values close to the ones needed for a global effect on the host galaxy (Deconto-Machado et al. 2023).

Appendix C.2: Accretion parameters

The black hole masses are computed assuming virial broadening for the emission lines: $M_{\text{BH}} = f r_{\text{BLR}} \text{FWHM}^2/G$, where f is the virial factor and r_{BLR} the radius of the emitting region (e.g., Vestergaard & Peterson 2006; Shen 2013). The dependence of f on the viewing angle has been parameterized by Mejía-Restrepo et al. (2018) as $f \approx (\text{FWHM}/4550)^{-1.17}$, and the r_{BLR} dependence on Eddington ratio by applying a correction to the standard scaling between r_{BLR} and optical luminosity at 5100 Å (Du & Wang 2019; MartínezAldama et al. 2020).

The main empirical correlation with Eddington ratio is the R_{FeII} prominence parameter (e.g., Sulentic et al. 2000b; Marziani et al. 2001; Sun & Shen 2015; Du et al. 2016; Panda et al. 2019), defined as the ratio between the fluxes of the FeII blend centered at 4570 Å and H β . The parameter R_{FeII} is one of the two main parameters (along with FWHM H β) defining the quasar Eigenvector 1 main sequence (Boroson & Green 1992; Sulentic et al. 2000b). The classical scaling law linking BLR distance r_{BLR} from AGN continuum to luminosity (Bentz et al. 2009) shows a dependence on Eddington ratio (MartínezAldama et al. 2020). A tight relation between r_{BLR} and luminosity can be recovered

once r_{BLR} is corrected, using the robust measurement of R_{FeII} in place of L/L_{Edd} . The following relation (Du & Wang 2019):

$$\log r_{\text{BLR}} \approx 17.063 + 0.45 \log L_{5100,44} - 0.35R_{\text{FeII}} [\text{cm}], \quad (\text{C.1})$$

yields:

$$\begin{aligned}\log M_{\text{BH}}(\text{H}\beta) &\approx 5.220 + 0.45 \log L_{5100,44} + \\ &0.83 \log \text{FWHM} - 0.35R_{\text{FeII}} [\text{M}_{\odot}].\end{aligned} \quad (\text{C.2})$$

Eq. C.2 implies a significant increase of the M_{BH} values for the sources with the narrowest profile with respect to the scaling law of Vestergaard & Peterson (2006), providing estimates in closer agreement with the ones obtained from more robust methods (DONOFRIO et al. 2024). The systematic M_{BH} uncertainty is estimated by computing the dispersion between the M_{BH} values computed from Eq. C.2 and three different scaling laws, of them two based on the H β line width (Vestergaard & Peterson 2006; Shen et al. 2024), and one on the H β luminosity (Greene & Ho 2005): $\delta \log M_{\text{BH}} \approx 0.17$, with a negligible bias between M_{BH} from Eq. C.2 and the average of the other scaling laws, $\delta \log M_{\text{BH}} \approx -0.05 \pm 0.20$. The uncertainty associated with the scaling law is still dominating with respect to the statistical uncertainties in line FWHM and in continuum flux measurement, $\lesssim 10\%$ at 1σ confidence level.

The bolometric correction (BC) was computed accounting for its dependence on luminosity (Runnoe et al. 2012). We utilize the BC parameterization by Netzer (2019) that are fairly consistent, at low luminosity, with the ones described for highly accreting quasars: for Eddington ratios in the range $\log L/L_{\text{Edd}} \sim -0.5 - 0.0$, at $\log \lambda L_{\lambda}(5100\text{\AA}) \sim 43 - 44 [\text{erg s}^{-1}]$ the bolometric correction has been estimated between 16 and 23 (Garnica et al. 2025) and 10 and 18.8 (Ferland et al. 2020). If the Garnica et al. and the Netzer (2019) bolometric corrections are applied to the present sample, the systematic difference in bolometric luminosity L is negligible, $\approx 12\%$. Results for optical and bolometric luminosity, and for M_{BH} and L/L_{Edd} are reported in Table C.4.

Table C.5 reports statistical and systematic linear fractional uncertainties for the accretion parameters. The main source of uncertainty is the systematic uncertainty associated with the different scaling laws employed for M_{BH} estimates. The uncertainty is apparently reduced with respect to earlier works (Vestergaard & Peterson 2006), but is still affecting heavily the M_{BH} and L/L_{Edd} estimates. If systematic and statistical errors are quadratically propagated (column Total in Table C.5), the uncertainties reach values $\gtrsim 70\%$ for the L/L_{Edd} , $\delta \log L/L_{\text{Edd}} \sim \pm 0.32$, an aspect that should be considered in any correlation analysis involving L/L_{Edd} .

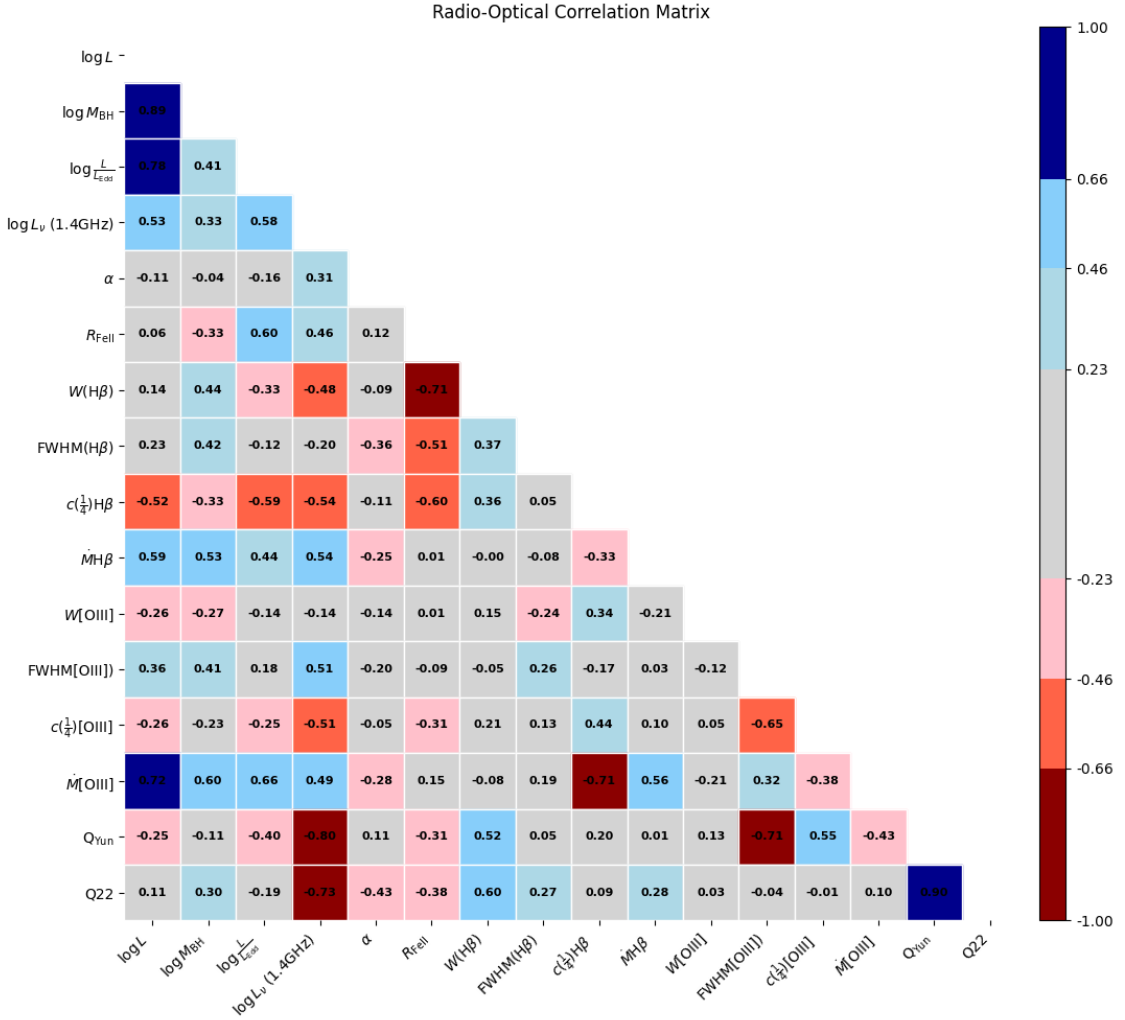


Fig. C.2: Correlation matrix (Pearson's) involving the main optical ($H\beta$ and $[\text{OIII}]\lambda 5007$), radio and IR derived parameters. The limits in the color ranges correspond to a statistical significance of $\pm 1, 2, 3\sigma$ for the Pearson's correlation coefficient computed for 18 objects. The parameters considered are in this order, the bolometric luminosity L , the black hole mass M_{BH} , the Eddington ratio L/L_{Edd} , the radio power at 1.4 GHz, the radio spectral index α , FeII prominence ratio R_{FeII} , the equivalent width of $H\beta$ (broad components), its FWHM and centroid displacement at one-half peak intensity $c(\frac{1}{2})$, the mass outflow rate measured from blueshift emission of $H\beta$, \dot{M} ; the equivalent width, FWHM, $c(\frac{1}{2})$, \dot{M} of the $[\text{OIII}]\lambda 5007$ line; the Q parameters defined according to [Yun et al. \(2001\)](#) and to Eq. 5.

Table C.1: Analysis of the H β and FeIIλ4570 emission features

Object	$f_{\lambda,5100}$	H β full broad profile (BC + BLUE)						FeIIλ4570						H β BC						H β BLUE																
		Flux	EW	FWHM	$c(\frac{1}{4})$	$c(\frac{1}{2})$	$c(\frac{3}{4})$	$c(\frac{9}{10})$	AI	KI	R_{FeII}	R_{FeII}	F/F(H β)	FWHM	F/F(H β)	FWHM	Shift	Skew	(1)	(2)	(3)	(4)	(5)	(6)	(7)	(8)	(9)	(10)	(11)	(12)	(13)	(14)	(15)	(16)	(17)	(18)
J00418+4021	3.59E-16	7.7E-15	23.2	1247	87	96	103	90	-0.002	0.336	1.32	0.8344	1257	0.166	3412	-2928	0.594																			
J00457+0410	7.03E-16	4.6E-14	67.6	4405	-668	-452	-162	-53	-0.175	0.355	1.18	0.6664	3413	0.334	5099	-1332	0.898																			
J00535+1241	5.77E-15	2.3E-13	41.0	1412	-83	-61	-60	-59	-0.019	0.327	1.83	0.9354	1408	0.065	1629	-2676	1.010																			
J10255+5140	1.44E-15	9.1E-14	60.1	1480	48	41	41	41	0.006	0.339	0.78	0.9970	1463	0.003	3634	-533	0.605																			
J11292-0424	1.56E-15	1.7E-13	115.9	2455	-55	-76	-53	-60	0.002	0.333	0.95	1.0000	2454	0.000																		
J11420+6030	2.75E-16	1.0E-14	41.7	1542	-625	-73	-78	-75	-0.293	0.243	2.12	0.9290	1522	0.071	4370	-2934	1.013																			
J12075+1506	1.20E-15	4.7E-14	66.4	2253	-11	98	112	95	-0.051	0.313	1.08	0.9515	2238	0.049	3775	-2598	0.393																			
J12091+5611	1.11E-16	2.7E-15	22.9	1186	-319	-265	-258	-266	-0.050	0.314	2.09	0.8363	1141	0.164	5069	-2095	1.010																			
J12366+5630	1.43E-16	3.5E-15	25.8	1973	-529	-289	-227	-201	-0.213	0.288	2.10	0.7662	1753	0.234	6200	-1158	0.392																			
J12562+5652	1.12E-14	4.3E-13	34.7	4480	-545	-321	-14	72	-0.165	0.316	1.93	0.8460	3599	0.154	3947	-2393	1.010																			
J13012+5902	1.91E-14	7.1E-13	56.8	3313	-601	-370	-89	-6	-0.215	0.319	1.37	0.7323	2523	0.268	3712	-1551	1.000																			
J14052+2555	2.26E-14	2.3E-12	105.7	2054	-94	-94	-94	-94	0.000	0.333	1.02	1.0000	2053	0.000																		
J14063+2223	5.80E-15	4.1E-13	58.9	1633	-132	-43	-24	-19	-0.077	0.301	1.10	0.9053	1528	0.095	3522	-1800	1.000																			
J14170+4456	1.02E-14	6.1E-13	66.0	2270	-448	-174	-59	3	-0.220	0.314	1.17	0.7320	1929	0.268	4098	-721	0.586																			
J14258+3946	1.07E-16	5.5E-15	49.4	1977	-148	13	2	-4	-0.093	0.368	1.10	1.0000	1975	0.000																		
J14475+3455	1.77E-15	3.7E-14	26.9	3862	-953	-863	-168	-122	-0.291	0.260	1.97	0.9981	2298	0.002	2572	-2957	0.459																			
J15455+4846	4.87E-16	3.5E-14	73.4	1794	-77	10	27	10	-0.052	0.310	1.06	0.8097	1723	0.190	6858	-3164	1.051																			
J17014+5149	2.62E-15	1.3E-13	46.9	2582	-329	-78	-71	-69	-0.105	0.296	1.19	0.9436	2528	0.056	4497	-2564	0.335																			

Notes. All measured quantities refer to rest-frame. Col. 1: Object coordinate name. Col. 2: specific flux at 5100 Å in units of erg s⁻¹ cm⁻² Å⁻¹. Cols. 3: flux in units of erg s⁻¹ cm⁻². Col. 4: equivalent width in Å. Cols. 5: FWHM of the H β full broad profile in km s⁻¹; Cols. 6-9: profile centroids at fractional peak intensity in km s⁻¹. Col. 10: asymmetry index; Col. 11: kurtosis index. See [Zamfir et al. 2010](#) for definition. Col. 12: ratio R_{FeII} ; Col. 13: fractional intensity of the H β BC; Col. 14: FWHM H β BC in km s⁻¹; Col. 15: fractional intensity of the blueshifted broad component BLUE; Col. 16: FWHM in km s⁻¹; Col. 17: peak shift (mode) of BLUE in km s⁻¹. Col. 18: skew of BLUE.

Table C.2: Profile analysis for [OIII] λ 5007Å

Object	Full profile (NC + SBC)								[OIII] NC				[OIII] SBC				
	Flux	EW	FWHM	$c(\frac{1}{4})$	$c(\frac{1}{2})$	$c(\frac{3}{4})$	$c(\frac{9}{10})$	AI	KI	$F/F([OIII])$	FWHM	Shift	$F/F([OIII])$	FWHM	$c(\frac{1}{2})$	Shift	Skew
(1)	(2)	(3)	(4)	(5)	(6)	(7)	(8)	(9)	(10)	(11)	(12)	(13)	(14)	(15)	(16)	(17)	(18)
J00418+4021	2.31E-15	7.00	1094	12	52	53	44	-0.040	0.446	0.89	1051	65	0.11	1641	-868	-875	0.97
J00457+0410	0.00E+00	0.00
J00535+1241	1.01E-13	18.36	1095	-1359	-823	-763	-750	-0.475	0.251	0.44	849	-718	0.56	2158	-1766	-1819	1.00
J10255+5140	9.45E-15	6.62	419	-24	-30	-20	-29	0.017	0.508	1.00	402	-30	0.00
J11292-0424	2.88E-14	20.50	501	-41	-31	-30	-30	-0.032	0.439	0.95	486	-20	0.05	445	-644	-669	0.97
J11420+6030	2.02E-16	0.82	1.00	206	303	0.00
J12075+1506	5.98E-15	8.89	1556	-979	-778	-389	-382	-0.537	0.242	0.32	617	-254	0.68	1609	-1176	-1163	1.02
J12091+5611	4.34E-16	3.94	321	-62	-62	-62	-60	-0.010	0.480	0.96	307	10	0.04	2335	-268	-224	1.01
J12366+5630	2.74E-15	21.89	328	-104	-44	-35	-43	-0.218	0.334	0.56	282	-21	0.44	750	-322	-286	1.01
J12562+5652	1.49E-14	1.21	1358	-2272	-2135	-2047	-1960	-0.324	0.449	0.00	1.00	1959	-2135	-1881	0.40
J13012+5902	3.26E-14	2.85	1220	-1115	-86	-75	-103	-0.011	0.364	0.30	1005	-86	0.70	2916	1823	-1262	5.25
J14052+2555	1.36E-13	6.31	1243	-185	-201	-282	-276	0.094	0.295	0.72	1500	-336	0.28	3000	-3043	-2376	0.10
J14063+2223	5.96E-14	9.20	803	-358	-261	-238	-231	-0.181	0.399	0.56	675	-215	0.44	495	-426	-912	4.85
J14170+4456	1.58E-14	1.61	494	-601	-604	-604	-609	0.021	0.413	1.00	494	-607	0.000
J14258+3946	8.91E-16	8.47	681	-54	-41	-39	-46	-0.017	0.451	0.79	683	30	0.21	3000	-2541	-1824	0.10
J14475+3455	1.62E-14	9.64	2472	-2454	-2416	-2363	-2335	-0.069	0.465	0.02	372	819	0.98	2718	-2416	-2264	0.83
J15455+4846	6.63E-15	14.77	3006	-2036	-2055	-2036	-2055	0.009	0.465	0.00	730	778	1.00	3000	-2055	-2088	1.02
J17014+5149	1.29E-14	5.08	5209	-1606	-1407	-1227	-1100	-0.169	0.747	0.31	916	778	0.69	4820	-3054	-2529	0.28

Notes. All measured quantities refer to rest-frame. Col. 1: Object coordinate name. Col. 2: [OIII] λ 5007 flux in units of ergs s^{-1} cm^{-2} . Col. 3: equivalent width in Å. Cols. 4: FWHM of the [OIII] λ 5007 full profile in km s^{-1} ; Cols. 5-8: profile centroids at $\frac{1}{4}, \frac{1}{2}, \frac{3}{4}, 0.9$ fractional peak intensity in km s^{-1} . Col. 9: asymmetry index; Col. 10: kurtosis index, as for H β . Col. 11: fractional intensity of the [OIII] λ 5007 NC in km s^{-1} ; Col. 13: peak shift of the [OIII] λ 5007 NC in km s^{-1} ; Col. 14: fractional intensity of the blueshifted semi-broad component SBC; Col. 15: FWHM of SBC in km s^{-1} ; Col. 16: SBC centroid at half maximum in km s^{-1} ; Col. 17: SBC peak shift (mode) in km s^{-1} . Col. 18: SBC skew.

Table C.3: Mass outflow rates and kinetic powers

Object	H β		[OIII] $\lambda 5007$	
	\dot{M}	$\dot{\epsilon}$	\dot{M}	$\dot{\epsilon}$
	[M $_{\odot}$ yr $^{-1}$]	[erg s $^{-1}$]	[M $_{\odot}$ yr $^{-1}$]	[erg s $^{-1}$]
J00418+4021	0.0251	1.16E+41	0.001	2.11E+39
J00457+0410	3.3547	7.05E+42
J00535+1241	0.1866	7.87E+41	0.233	1.31E+42
J10255+5140	0.0004	3.32E+38
J11292-0424	0.0000	0.00E+00	0.003	5.39E+39
J11420+6030	1.9106	8.84E+42
J12075+1506	2.9473	1.21E+43	1.194	4.49E+42
J12091+5611	0.1955	6.46E+41	0.0005	3.88E+38
J12366+5630	0.5111	9.33E+41	0.087	8.94E+40
J12562+5652	0.3743	1.41E+42	0.038	2.60E+41
J13012+5902	69.596	1.70E+44	4.924	2.87E+43
J14052+2555	0.0000	0.00E+00	1.947	1.90E+43
J14063+2223	0.8687	2.47E+42	0.070	9.60E+40
J14170+4456	1.8542	2.11E+42
J14258+3946	0.0000	0.00E+00	0.063	5.14E+41
J14475+3455	9.7100	4.53E+43	7.902	6.11E+43
J15455+4846	3.6547	1.82E+43	1.196	7.86E+42
J17014+5149	1.8024	7.29E+42	1.34	1.31E+43

Table C.4: Accretion parameters

Object	$\log \lambda L_{\lambda}(5100\text{\AA})$	$\log L_{\text{bol}}$	$\log M_{\text{BH}}$	$\log L_{\text{bol}}/L_{\text{Edd}}$
J00418+4021	43.33	44.67	7.03	-0.54
J00457+0410	44.99	45.99	8.19	-0.37
J00535+1241	44.38	45.51	7.37	-0.03
J10255+5140	43.53	44.82	7.36	-0.72
J11292-0424	43.84	45.07	7.63	-0.73
J11420+6030	45.04	46.03	7.59	0.27
J12075+1506	45.71	46.57	8.39	0.00
J12091+5611	44.31	45.45	7.17	0.11
J12366+5630	44.74	45.79	7.51	0.10
J12562+5652	44.36	45.49	7.66	-0.35
J13012+5902	46.59	47.27	8.73	0.36
J14052+2555	45.81	46.65	8.43	0.04
J14063+2223	44.79	45.83	7.83	-0.18
J14170+4456	45.17	46.14	8.07	-0.10
J14258+3946	44.38	45.50	7.74	-0.42
J14475+3455	45.80	46.64	8.13	0.33
J15455+4846	44.86	45.89	7.92	-0.21
J17014+5149	45.34	46.27	8.23	-0.14

Notes. Col. 1: Object coordinate name. Col. 2: decimal logarithm of luminosity at 5100 Å in units erg s $^{-1}$. Col. 3: bolometric luminosity in units erg s $^{-1}$, from $\log \lambda L_{\lambda}(5100\text{\AA})$ applying the bolometric correction by [Netzer \(2019\)](#). Col. 4 is the logarithm of black hole mass in units of M $_{\odot}$. Col. 5: Eddington ratio.

Table C.5: Statistical and systematic linear fractional uncertainties for the accretion parameters

Parameter	Statistical	Systematic	Total
FWHM	0.100	...	0.100
$\lambda L_{\lambda}(5100\text{\AA})$	0.200	...	0.200
M_{BH}	0.224	0.602	0.642
BC	...	0.346	0.346
L	0.200	0.346	0.399
L/L_{Edd}	0.224	0.694	0.729